Development of crack monitoring system for concrete structures

Using magnetic field variation

Thesis report

Kanhai P Joshi

Delft University of Technology

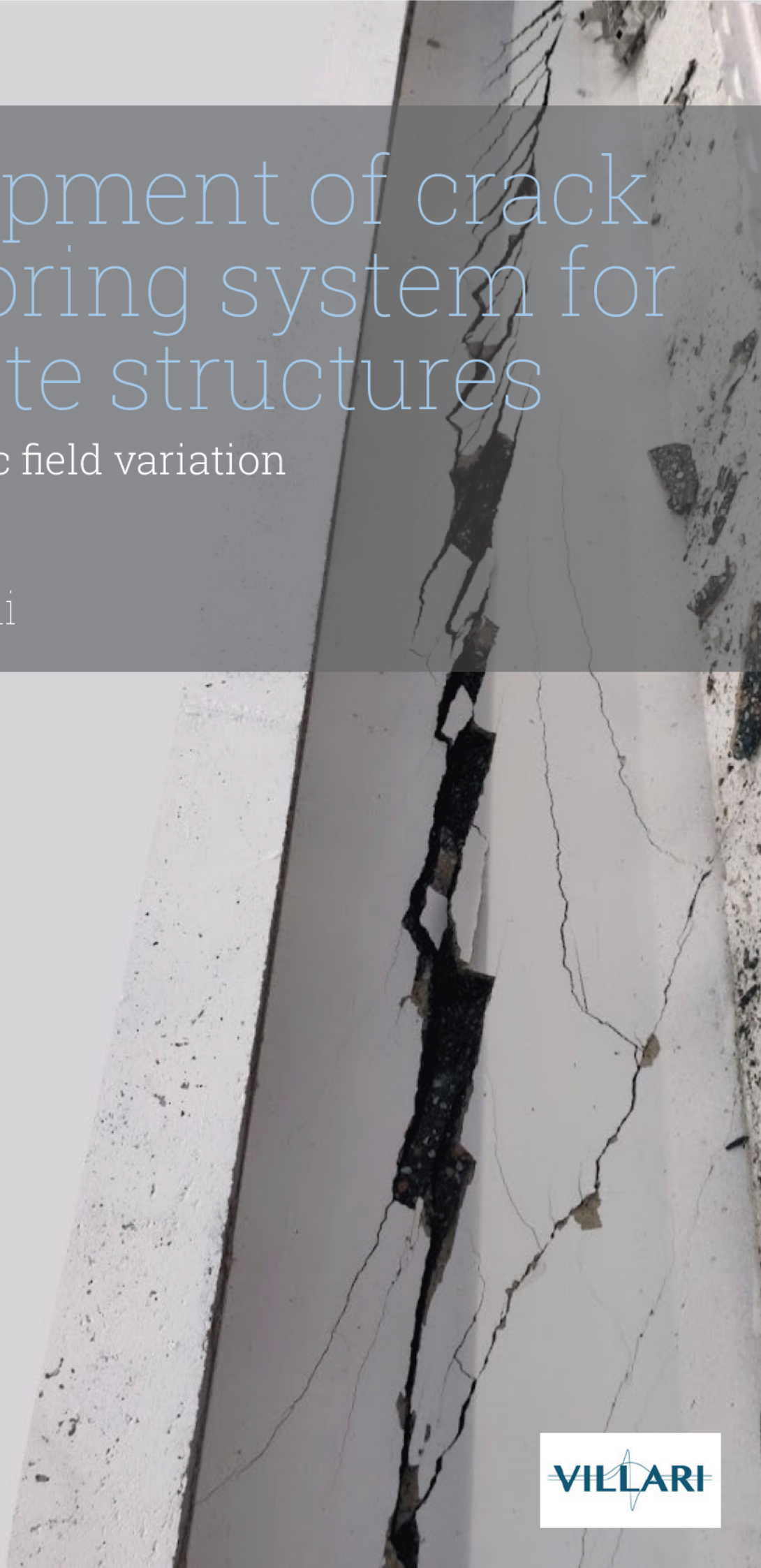

TU Delft

VILLARI

Development of crack monitoring system for concrete structures

Using magnetic field variation

by

Kanhai P Joshi

Student number 5378702

Committee members:	Dr. M. (Mohammad) Fotouhi
	Dr. O. (Oguzhan) Copuroglu
	Dr. S.C. (Sandra) Barbosa Nunes
Company supervisor:	Olivier Baas (Villari B.V.)
Faculty:	Faculty of Civil engineering and Geo-sciences, Delft

TU Delft

VILLARI

Acknowledgement

I would like to express my sincere gratitude to all those who have contributed to the successful completion of this study.
I am immensely grateful to Olivier Bass for providing me with this wonderful opportunity. Working with him to develop the monitoring system has been an incredibly insightful experience. His constant guidance, support, and unwavering confidence in me have made the journey both enriching and enjoyable.
I am deeply thankful to my supervisor Mohammad Fotouhi for always being supportive and for recognising my true potential. I am also grateful for his valuable guidance and mentorship throughout my research journey. I would also like to extend my appreciation to Sandra Barbosa Nunes and Oguzhan Copuruglu for their valuable insights and creative suggestions. Their expertise and knowledge have been instrumental in shaping the direction of this study.
Furthermore, I would like to express my gratitude to my friends here in the Netherlands and back in India for their invaluable friendship and encouragement, which helped me navigate through the ups and downs of this academic endeavor.
Lastly, I would like to thank my parents and my brother for their unwavering support, confidence and love for me.

Kanhai P Joshi
Delft, June 2023

Abstract

Despite stringent safety standards, concrete is prone to various forms of deterioration over time, and the occurrence of cracks is not uncommon. Therefore, the detection and monitoring of deformations in concrete are essential to mitigate the risks associated with structural failure. Implementing a real-time Structural Health Monitoring (SHM) system can play a crucial role in identifying early signs of damage, such as corrosion in reinforcement, thus enhancing the efficiency of maintenance and repair interventions and ultimately prolonging the lifespan of the structure. The data collected through SHM techniques also contribute to the validation of design practices employed in the structure and further advancements in the field. In a broader context, the integration of SHM supports the development of sustainable infrastructure, ensuring the longevity and safety of concrete structures.

Along with visual inspection, SHM techniques are deployed to conduct a thorough analysis of structural behaviour. However, many traditional methods involve tedious installation processes. Several techniques utilize a wide spectrum of radiations, such as ultraviolet pulses, infrared radiations, and X-rays, and rely on sophisticated equipment that demands trained personnel for data analysis. In this study, a novel approach is proposed for SHM by utilizing magnetic fields for crack monitoring. Currently, this technique is used to monitor cracks in steel structures.

The aim of this work is to explore and adapt this idea to integrate the sensor system into the field of structural health monitoring for concrete structures. The scientific contributions made in this study include the investigation of the effects of crack propagation on the magnetic field, the modeling of the behavior using analytical and numerical methods, the construction of a prototype, the validation of the structural health monitoring technique, and the demonstration of the feasibility of this method.

Contents

List of Figures

List of Tables

1 Introduction

1.1. Background

The use of concrete dates back to around 700 BC, making it one of the oldest construction materials. It has gained popularity as the most widely used material in construction due to its affordability and high-strength characteristics. However, concrete is inherently prone to cracking due to its brittle nature. Once cracks begin to appear, continuous monitoring of concrete structures becomes necessary. Although some degree of cracking is anticipated during the design phase, exceeding the permissible limits compromises the stability, safety, and overall design of the structure. Hence, there is an increasing interest in adopting structural health monitoring techniques [1]. In this context, developing an economical and small-scale technique for crack monitoring holds significant value. Such a technique can provide timely information for making informed decisions and help prevent potential catastrophes in the future.

Concrete structures can be monitored using various techniques. Currently, X-rays, gamma radiation, and thermography are commonly used to detect anomalies in the structure. Additionally, the detection and monitoring of corrosion in rebars are widely performed. However, these techniques have their limitations which are discussed in the chapter ahead. Many modern monitoring techniques focus on using sensors embedded in the concrete. This report proposes a novel crack monitoring system and details the current technologies for crack monitoring systems. It is found that research is being conducted on various types of sensors for structural health monitoring (SHM). This is driven by the need to detect and assess small-scale damage, as current technologies often fail to do so. Structural monitoring is typically performed only when damage to a primary component is evident, indicating the need for repair and maintenance. However, this approach can lead to system failure in systems without redundancy. Therefore, a low-cost, small-sized monitoring system with wireless capabilities is proposed. This system would enable the monitoring of structural elements at risk of damage.
Furthermore, monitoring techniques, such as acoustics, have emerged to encompass the entire structure. These approaches involve developing models that can predict strain patterns associated with new damage in the structure based on

data collected on the structure's behaviour. However, it should be noted that the accuracy of predicting damage is limited, as the neural network can only make predictions when matched with the exact training model [2]. Additionally, the complexity of the technique is increased by the requirement for trained individuals to interpret the data.

The monitoring system: RFV-2 proposed in this report covers a monitoring area of approximately $15cm^2$. Monitoring is performed locally, giving real-time data on how the structure behaves. Further, multiple sensors can be placed throughout the structure. As they are wireless, there is no requirement for physical inspection after installation. The battery life is five years, making it an ideal tool for long-term monitoring.

In this study, Anisotropic Magneto Resistance sensors are used to monitor crack behaviour in concrete structures. The monitoring system works as a non-destructive test. This monitoring system includes a setup which consists of a sensor strip and a magnet. The setup is installed after visual inspection. Placing the setup at zones where cracking is highly anticipated is also possible. Measurements of the sensors will vary based on the crack propagation pattern. Since the sensors measure a magnetic field, crack propagation in all three directions should cause a change in the magnetic field. Due to crack tip propagation also, the magnetic field is affected.

1.2. Objectives

The objectives of this thesis are outlined such that the concept of the monitoring system can be realised; the system can be validated and integrated into concrete crack monitoring. Therefore, the objectives can be formalised as listed below:

1. Optimal magnet selection for accurate crack monitoring: The objective is to utilise finite element models to study magnetic fields, determining the appropriate magnet size within the sensor's range to minimise the monitored area. This optimisation aims to enable precise identification of crack propagation within a pre-defined, smaller region.
2. Establishing a reference setup to investigate magnetic field behaviour: The objective is to construct a setup to investigate the behaviour of magnetic fields based on the proof of concept, thereby establishing experimental results that can serve as a reference for future studies.
3. Utilisation of the monitoring system for crack monitoring in concrete specimens: Implement the monitoring system within an experimental setup to detect cracks on two types of concrete specimens: a small-scale and a large-scale specimen.

1.3. Research questions

The main research focus of the thesis is formulated as follows:
Developing a monitoring system using AMR sensors for crack monitoring in concrete structures.
The following fundamental questions that must be addressed are:

1. What are the most suitable geometry and material of magnet for the proposed monitoring system?
2. How does the magnetic field behave during the cracking process of concrete?
3. What is the level of precision of the sensor?

1.4. Methodology

In order to develop an economical and easy-to-analyse crack monitoring system, an Anisotropic Magneto Resistive (AMR) sensor is used. It finds application in position detection in ferromagnetic materials like steel. The first question is whether this sensor type is compatible with concrete. Since concrete does not affect the magnetic field, it is a first impression that AMR sensors are unsuitable. However, this problem is fixed by introducing a magnetic field along with the sensor. Now, another obstacle occurs as to how this system will function. The answer lies in the fundamental principle of magnetism. The magnetic field follows the inverse square law with distance. This means the magnetic field is inversely proportional to the square of the distance as shown in section 1.4. According to this law, the intensity of the magnetic field reduces as the distance from the source of the field increases.

$$B \propto \frac{1}{x^2} \tag{1.1}$$

$B =$ Magnetic field
$x =$ Distance

It is necessary to ascertain what magnets best implement the above principle within the monitoring system. For this, finite element models are developed to comprehend the field behaviour in a 3D environment.
The methodology employed in this research as shown in figure 1.1 consists of the following steps:

1. Literature Review:
   A comprehensive literature review is conducted to identify current techniques used for concrete crack monitoring and to understand the concrete crack mechanism and the functioning of Anisotropic Magneto-Resistive (AMR) sensors.
2. Analytical and Numerical Analysis:
   Analytical calculations are performed to determine the appropriate magnet size. Subsequently, experiments are conducted, followed by a comparative study to assess the system's effectiveness under various conditions.

3. Experiments performed to understand the behaviour of the magnetic field are as follows:

    - Moving Table Experiment:
      In this experiment, the sensor and magnet are positioned at a predetermined distance from each other. A crack opening is simulated using a moving table. The experiment is repeated multiple times to demonstrate repeatability.
    - Concrete Prisms:
      Concrete prisms measuring 160mm x 40mm x 40mm are subjected to a four-point bending test. A single crack is initiated at the bottom of the prism and propagates towards the top. The monitoring system, along with Linear Variable Differential Transducers (LVDTs), is employed to monitor the behaviour of the crack. The primary focus is on crack propagation, although the overall data also provide promising results for crack detection.
    - Shear Failure:
      For this experiment, 15-meter girder beams are utilised. The beams are subjected to shear failure, and sensors are placed on the beams immediately after crack detection. The crack propagation is monitored until the complete failure of the beam. Two beams are used to test the monitoring system, and the results are validated through Digital Image Correlation and LVDT measurements, among other monitoring methods.

4. Findings and recommendations: Conclusions, limitations, and recommendations are derived by analysing the results and observations obtained from the experimental, analytical, and numerical analysis.

After following the procedure illustrated above, a detailed analysis is carried out to determine the accuracy of the monitoring system and optimal design of the sensors based on the current technology already implemented. The following section provides an overview of the report to understand the system's working.

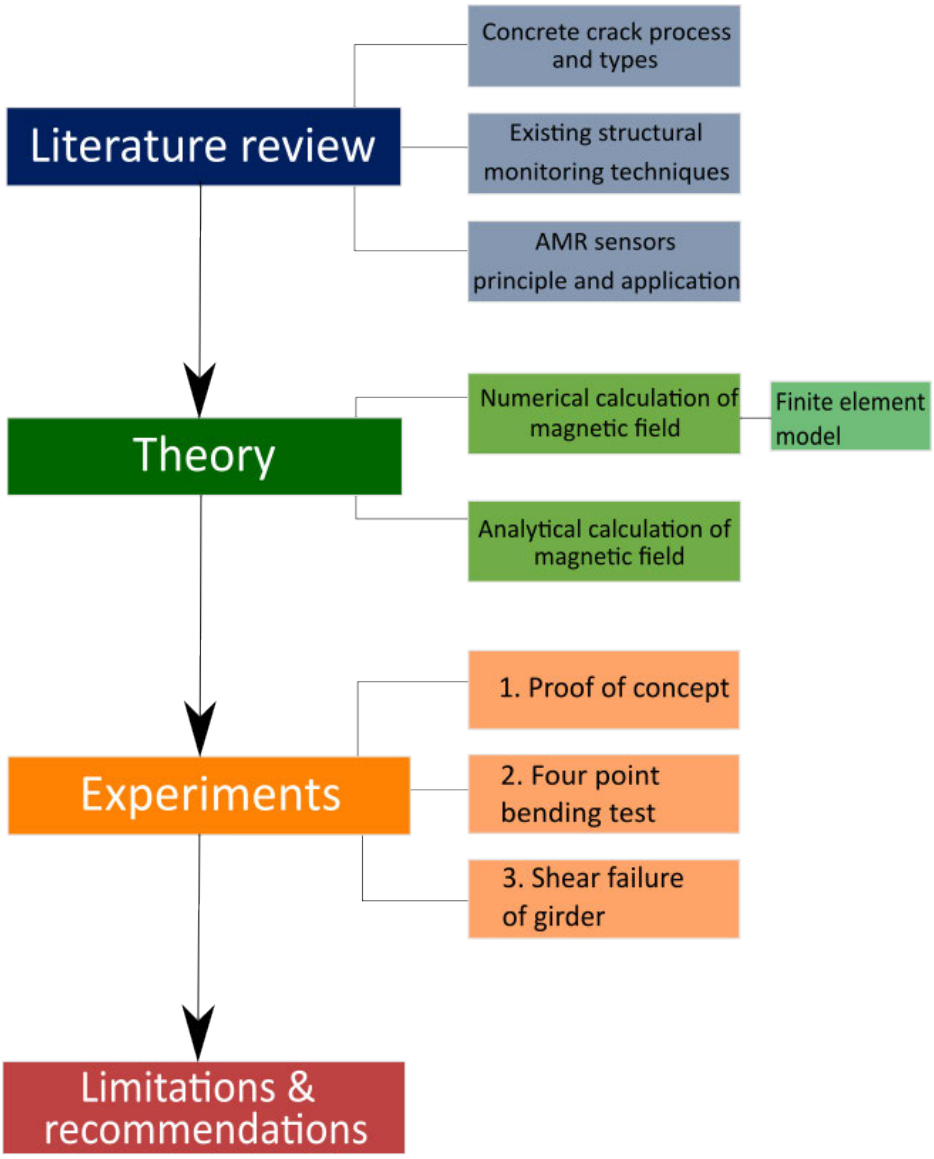

Figure 1.1: Study procedure: Schematic

1.5. Outline

The report consists of eight parts.
Chapter 1 offers a concise overview of the sensor system and its integration with structural health monitoring. It also introduces the research questions and the subsequent methodology employed to address them.

Chapter 2 details the literature review of available technologies in structural health monitoring. A wide range of systems has been carefully studied to understand the problems different techniques face. By doing so, the obstacles are considered, and novel ideas are explored in the following chapters.

Chapters 3 and 4 delve into the theoretical foundation behind the monitoring sys-

tem - RedFox Villari-2 (RVF-2). To fully comprehend the working principles and reasoning behind each design and practical choice, an in-depth study of reinforced concrete's sensors, magnetic field, and the cracking process is conducted. These topics are further divided into sub-chapters. The section dealing with sensors elaborates on the working principles of the developed monitoring system.

Chapter 5 explains the experimental procedure devised to support the proof of concept. The results of experiments using a moving table are discussed. No concrete specimen is used in this experiment; hence, the material properties are yet to be studied. These experiments are performed multiple times to establish repeatability.

Chapter 6 focuses on the four-point bending test to generate a single crack specimen. The crack evolution is studied using the monitoring system, and for validation purposes, LVDTs are employed in this experiment. The chapter provides detailed information about the setup and the necessary assumptions, followed by a discussion of the results.

Chapter 7 presents an experimental study of a beam undergoing shear failure. The RVF-2 monitoring system is placed immediately after crack initiation. Data is collected until failure and validated using Digital Image Correlation. This experiment provides insights into the practical applicability of the system.

Chapter 8 provides conclusions based on the theoretical background established in chapters 3 and 4 and the experiments conducted in chapters 5 to 7. It offers insights into the usability of the monitoring system based on the recommendations provided.

2

Concrete cracks

Understanding the damage evolution in concrete before moving on to methods for monitoring concrete cracking is essential. Cracks in concrete can occur before hardening due to differential temperature, which causes the development of shrinkage stresses. After concrete hardening, cracks can be caused due to Imposed deformations (differential settlements), creep, shrinkage and dead and live loads. Studying the various aspects of cracking falls outside the scope of this research. However, for establishing the principles and working of the monitoring system, cracking associated with beam bending is discussed in detail.

2.1. Crack mechanism

Various possibilities exist which can cause a concrete structure to crack. Concrete can withstand compressive forces while having a lower tensile strength. Therefore, cracks develop when the stresses on the structure exceed the concrete tensile stress. Cracking is a comprehensive phenomenon. According to fracture mechanics, any crack pattern can be described by three basic modes of fracture - opening, shearing and tearing [3]. These cracking modes will be handy in defining tensile, in-plane and out-of-plane shear cracks.

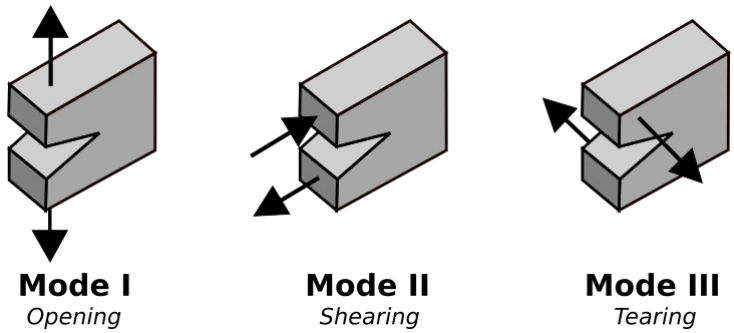

Figure 2.1: Modes of a crack in concrete

When subjected to loading, concrete initially behaves like a linear elastic material. Micro cracks develop at the weakest region, which coalesces to form a macro

crack. On the onset of cracking, the linear mechanics will no longer hold as a series of micro cracks develop, which causes strain localisation [4], [5]. This region ahead of the crack tip is called the fracture process zone. This non-linear process zone will depend on the aggregate characteristics, size of the aggregates and specimen size [6]. When subjected to further loading, the micro-cracks combine and form a macro crack. Strain gauges do not give optimum results as they measure an average strain value. Sensors with higher sensitivity have to be used to capture the occurrence of micro cracks. These sensors will be addressed in the next section.

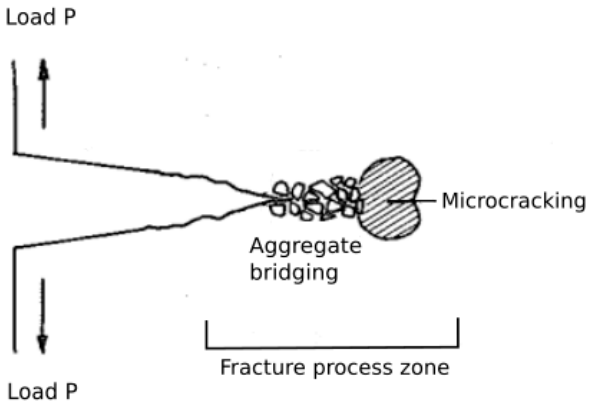

Figure 2.2: Fracture process zone in case of tensile loading [6]

2.1.1. Flexural cracks based on a tension model (Mode I)

Consider a reinforced concrete element which is loaded in tension. Before forming a crack in the tension bar, the strain in the reinforcement and concrete will be equal. Force contribution of reinforcement and concrete will be:

$$\begin{aligned} N_s &= E_s A_s \epsilon \\ N_c &= E_c A_C \epsilon \end{aligned} \tag{2.1}$$

Therefore, total force where $\alpha_e = E_s/E_c$ and $\rho = A_s/A_c$ (reinforcement ratio) will be;

$$\begin{aligned} N_{total} &= N_s + N_c \\ &= E_s A_s \epsilon + E_c A_c \epsilon \\ &= E_C A_c (1 + \alpha_e \rho) \epsilon_c \end{aligned} \tag{2.2}$$

At certain moments, when the strain ϵ_c increases such that the tensile stress in the concrete is equal to the tensile strength of the concrete. The crack will form where the tensile strength of the concrete is lowest. When the load is applied, elastic deformation will occur, and micro-cracks will develop. Once the load reaches a

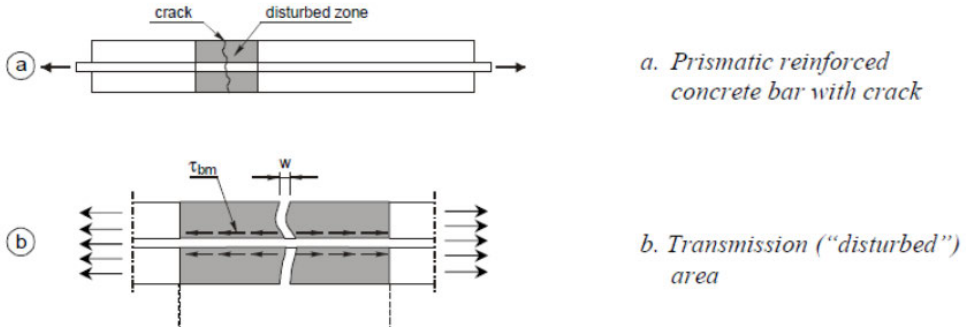

Figure 2.3: Crack formation [7]

point such that the tensile strength of concrete is reached, these micro-cracks will combine to form a major crack as presented in figure 2.3. When the concrete is fully cracked, the reinforcement carries the stress in concrete,$\sigma_{ct} = 0$ and the load. The tension bar is said to fail once the reinforcement yields.
When a beam is subjected to a four-point bending test, the bottom zone of the beam is subjected to tension. Hence, a tension model can be adopted for a flexure member[8].

2.1.2. Shear cracks (Mode II)

Generally, for concrete, the cracks change from tensile crack (mode-I crack) to shear crack as the loading is continued. From previous studies, it is found that in the initial cracking phase, tensile cracks appear, followed by a combination of tensile and shear cracks and finally, the shear cracks are dominant for failure [9]. However, only sometimes do tensile cracks lead to shear cracks. The shear forces in the structure ultimately cause the shear cracks [10].
In Figure 2.4, it is evident that flexure cracks emerge in the tension zone (located at the bottom region of the beam) and propagate upward. These cracks exhibit an inclined orientation due to the presence of shear forces. The phenomenon of aggregate interlock, characterized by the mechanical interlocking of coarse aggregates, effectively prevents sliding and offers resistance against shear forces within the compression zone. Additionally, reinforcement bars play a crucial role in transferring shear forces between different sections of the concrete, thereby providing further resistance. As the shear force increases, diagonal cracks form, inducing tension in the surrounding areas [11]. The following equations are provided in Eurocode-2.

1. Shear strength of concrete beams without shear reinforcements is calculated as below:

$$\begin{aligned} V_{Rd,c} &= [C_{Rd,c}k(100\rho_1 f_{ck})^{1/3} + k_1\sigma_{cp})]b_w d \\ &\leq (v_{min} + k_1\sigma_{cp})b_w d \end{aligned} \tag{2.3}$$

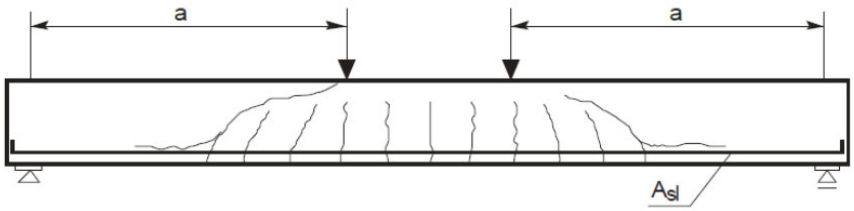

Figure 2.4: Shear failure of a beam [7]

where,
$k = 1 + \sqrt{200/d} \leq 2.0$
$\rho_1 = A_{sl}/b_w d \leq 0.02$
A_{sl} = area of tensile reinforcement
f_{ck} is compressive strength of concrete in MPa
$\sigma_{cp} = N_{Ed}/A_c < 0.2 f_{cd}(MPa)$
b_w = smallest width of cross-section due to tensile area (mm)
d = depth of cross-section (mm)
The following are provided in the national annex. However, Eurocode 1992-1-1 provided recommended values are:
$C_{Rd,c} = 0.18/\gamma_c$
$k_1 = 0.15$
$v_{min} = 0.035 k^{3/2} f_{ck}^{1/2}$

2. For concrete beams designed with shear reinforcement, the shear strength is given by:

   - Vertical shear reinforcement:
     $V_{Rd,s} = min\left\{ \frac{A_{sw}}{s} z f_{ywd} cot(\theta), \frac{\alpha_{cw} b_w z v_1 f_{cd}}{cot(\theta)+tan(\theta)} \right.$
   - Inclined shear reinforcement:
     $V_{Rd,s} = min\left\{ \frac{A_{sw}}{s} z f_{ywd}(cot(\theta) + cot(\alpha)) sin(\theta), \alpha_{cw} b_w z v_1 f_{cd} \frac{cot(\theta)+cot(\alpha)}{(1+cot^2(\theta))} \right.$

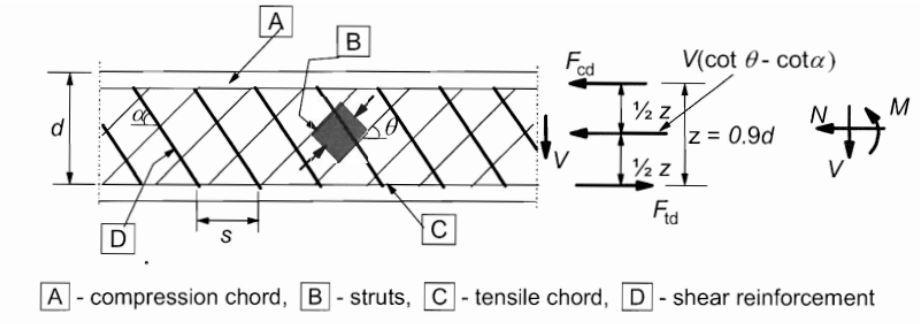

Figure 2.5: Truss model and parameters for shear reinforced beam [7]

where,
$A_{sw} =$ cross-sectional area of the shear reinforcement
s = spacing of the stirrups

f_{ywd} = design yield strength of the shear reinforcement
v_1 = strength reduction factor for concrete cracked in shear
α_{cw} = coefficient for state of the stress in the compression chord
$\alpha =$ angle between shear reinforcement and the beam axis perpendicular to the shear force
Recommended values for v_1 and α_{cw} are specified in the national annex.
θ = angle between the concrete compression strut and the beam axis perpendicular to the shear force
b_w = minimum width between the tension and the compression chords
z = inner lever arm = $0.9d$

2.2. Code provision for cracking

Crack-width control

Provisions are made in the design of concrete structures to control cracking to provide durability and aesthetics. According to Eurocode 1992-1-1 section 7.3 [12], cracks are permitted in the structure as long as it does not interfere with the functioning of the structure and does not compromise the safety of the structure. This allowance in cracking is given based on the exposure class. The exposure classes presented in figure 2.6 are determined based on the environmental conditions and the conditions to which the structure will be subjected during its operational life.

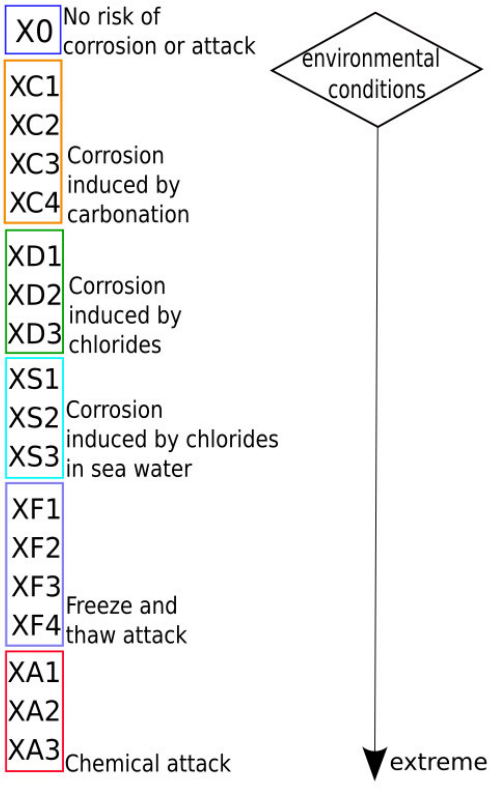

Figure 2.6: Exposure classes

The maximum crack-width allowance is based on the exposure classes to which the structure is subjected. Figure 2.7 illustrates the crack width allowance. For the experiments performed to develop the SHM system using RFV-2 sensors, this range for crack width is scrutinised. Cracking in concrete can be attributed to various factors. Over time, the combined effects of creep and shrinkage can lead to cracks. Reinforced concrete that is prone to corrosion can develop cracks as well. Cracks may also appear when a structure is subjected to overloading, exceeding its intended capacity. Additionally, concrete can crack due to differential settlements and the influence of thermal effects.

Table 7.1N Recommended values of w_{max} (mm)

Exposure Class	Reinforced members and prestressed members with unbonded tendons	Prestressed members with bonded tendons
	Quasi-permanent load combination	Frequent load combination
X0, XC1	0,4[1]	0,2
XC2, XC3, XC4	0,3	0,2[2]
(AC2) XD1, XD2, XD3, XS1, XS2, XS3 (AC2)		Decompression

Note 1: For X0, XC1 exposure classes, crack width has no influence on durability and (AC1) this limit is set to give generally acceptable appearance. In the absence (AC1) of appearance conditions this limit may be relaxed.

Note 2: For these exposure classes, in addition, decompression should be checked under the quasi-permanent combination of loads.

Figure 2.7: Recommended maximum crack-width

Cracks develop in the tension zone. Therefore, minimum reinforcement needs to be provided to control the crack widths. Minimum required reinforcements can be calculated using the equilibrium in tensile force in concrete before cracking and tensile force in the reinforcement (EN1992-1-1 cl.7.3.2). In case of a structural member of depth up to 200 mm subjected to bending without significant axial tension, the reinforcement size and spacing can be estimated using the table 2.8 and 2.9.

Steel stress[2] [MPa]	Maximum bar size [mm] w_k= 0,4 mm	w_k= 0,3 mm	w_k= 0,2 mm
160	40	32	25
200	32	25	16
240	20	16	12
280	16	12	8
320	12	10	6
360	10	8	5
400	8	6	4
450	6	5	-

Notes: 1. The values in the table are based on the following assumptions:
(AC1) c = 25mm; $f_{ct,eff}$ = 2,9MPa; h_{cr} = 0,5h; (h-d) = 0,1h; k_1 = 0,8; k_2 = 0,5; k_c = 0,4; k = 1,0; k_t = 0,4 and k_4 = 1,0 (AC1)
2. Under the relevant combinations of actions

Figure 2.8: Maximum bar size, Table 7.2N [12]

Steel stress[2] [MPa]	Maximum bar spacing [mm] w_k=0,4 mm	w_k=0,3 mm	w_k=0,2 mm
160	300	300	200
200	300	250	150
240	250	200	100
280	200	150	50
320	150	100	-
360	100	50	-

Figure 2.9: Maximum spacing, Table 7.3N [12]

Concrete cover

The concrete cover is the distance from the outer fibre to the reinforcement in the concrete. Corrosion of the reinforcement has been a significant cause of structural damage leading to failure [13]. The concrete cover is provided to protect the reinforcement against aggressive environmental conditions. Reinforcement bars are prone to corrosion. Corrosion causes the concrete around the reinforcement to deteriorate and weaken the bond between the reinforcement and concrete. This process is illustrated in figure 2.10. The concrete cover is calculated to provide

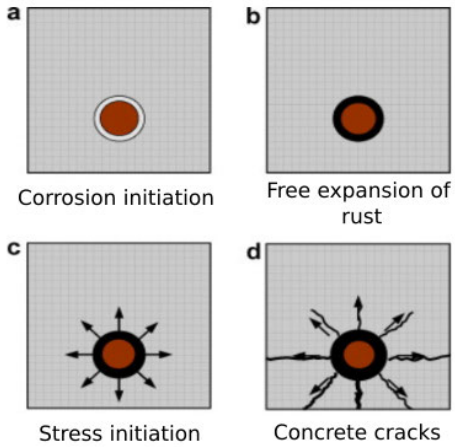

Figure 2.10: Crack mechanism due to corrosion [14]

sufficient bond transfer and corrosion and fire resistance. Guidelines for providing concrete cover are provided in EN1992-1-1, clause 4.4.1.

$c_{min} = max\{c_{min,b}; c_{min,dur} + \Delta c_{dur,\gamma} + \Delta c_{dur,st} + \Delta c_{dur,add}; 10mm\}$

The values of $c_{min,b}$ and $c_{min,dur}$ are based on the exposure class, as shown in the figures 2.11 to 2.13. Values of $\Delta c_{dur,\gamma}, \Delta c_{dur,st}, \Delta c_{dur,add}$ are given in the national annex (recommended value in Eurocode is 0mm).

Bond Requirement	
Arrangement of bars	Minimum cover $c_{min,b}$*
Separated	Diameter of bar
Bundled	Equivalent diameter (ϕ_n)(see 8.9.1)
*: If the nominal maximum aggregate size is greater than 32 mm, $c_{min,b}$ should be increased by 5 mm.	

Figure 2.11: Concrete cover based on bond requirement of reinforcements (c_min, b)

Environmental Requirement for $c_{min,dur}$ (mm)							
Structural Class	Exposure Class according to Table 4.1						
	X0	XC1	XC2 / XC3	XC4	XD1 / XS1	XD2 / XS2	XD3 / XS3
S1	10	10	10	15	20	25	30
S2	10	10	15	20	25	30	35
S3	10	10	20	25	30	35	40
S4	10	15	25	30	35	40	45
S5	15	20	30	35	40	45	50
S6	20	25	35	40	45	50	55

Figure 2.12: Concrete cover for durability in case of reinforced concrete structures (c_min, dur)

Environmental Requirement for $c_{min,dur}$ (mm)							
Structural Class	Exposure Class according to Table 4.1						
	X0	XC1	XC2 / XC3	XC4	XD1 / XS1	XD2 / XS2	XD3 / XS3
S1	10	15	20	25	30	35	40
S2	10	15	25	30	35	40	45
S3	10	20	30	35	40	45	50
S4	10	25	35	40	45	50	55
S5	15	30	40	45	50	55	60
S6	20	35	45	50	55	60	65

Figure 2.13: Concrete cover for durability in case of prestressed concrete structures (c_min, dur)

2.3. Structural health monitoring (SHM)

2.3.1. Introduction

Structural health monitoring (SHM) is becoming an essential aspect of the construction industry as the design life of many structures is reaching the repair phase. It is essential to monitor them to ensure their continued safety and functionality. The amount of cement production has increased since the early 2000s. This directly points to the fact that the vastness of infrastructure has also widened. This can be interpreted from the figure 2.14. These structures from the early 2000s are likely to reach half- or full-design life; hence, they must be monitored for cracks. Hence, developing a system that can be economical and user-friendly is essential.

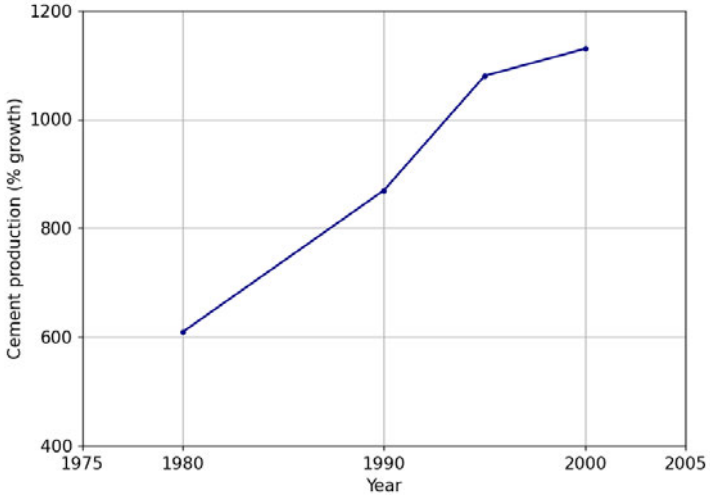

Figure 2.14: Infrastructure growth based on cement production [15]

Traditionally, structural integrity analysis heavily relied on visual inspection, which has inherent limitations as it can only detect damage at a macroscopic level, often missing the early stages of micro-level damage. To overcome these limitations, non-destructive evaluation (NDE) techniques emerged as a subset of Structural Health Monitoring (SHM). NDE involves applying non-destructive techniques to specific locations in a concrete structure. However, due to the heterogeneous nature of concrete and the influence of factors such as micro-structure and applied loading conditions, the patterns and locations of cracks can vary significantly. Therefore, there is a need for a comprehensive system that can collect data on structural health simultaneously from multiple locations on the structure.
Structural Health Monitoring (SHM) techniques have emerged as a solution to continuously collect and analyze real-time data from structures. These systems enable the detection of anomalies occurring in a structure, offering early warning signs of potential damage. In the context of this thesis, the monitoring system RFV-2 is employed for monitoring cracks. Various sensors play a crucial role in SHM systems and contribute to safer structural designs further making the infrastructure sustainable. With advancements in technology and the integration of the Internet of Things (IoT), wireless sensors have become widely utilized in structural

health monitoring systems [1]. Figure 2.15 provides comprehensive applications of IoT for structural health analysis.
In civil engineering, structures are typically designed using conservative approaches to ensure ”low-risk” structures. Structural engineers have incorporated their experience into design practices and developed safety factors to meet these objectives. Visual inspection and NDE are commonly employed to monitor structures for responses to various load factors. The utilization of sensors in SHM for inspection purposes is often referred to as ”civionics” [16].

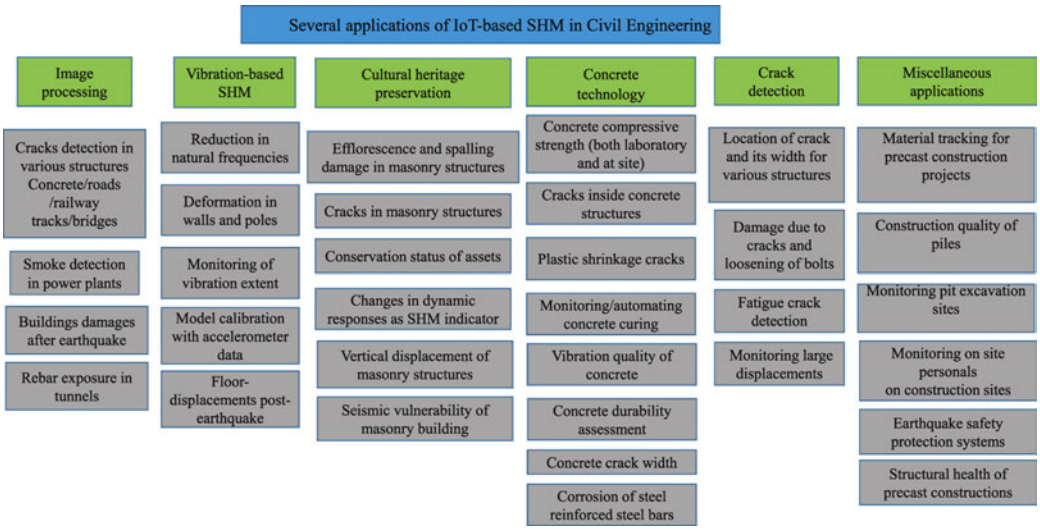

Figure 2.15: Applications of IoT in SHM [17]

The field of ”civionics” continues to evolve, providing engineers with valuable insights and data-driven decision-making tools for ensuring the long-term performance and safety of civil engineering structures.

2.3.2. Techniques and methods

In this section, the current SHM techniques are discussed. The response of any structure depends on the mass, stiffness and damping values. The formation of cracks will cause changes to these parameters. By taking into account the changes in strain and energy dissipation, several methods are used to detect cracks. The sensors' primary application in crack monitoring focuses on determining the propagation of cracks and estimating the crack width.

1. *Strain gauge:*
   Electric and mechanical strain gauges are popular techniques to measure the strain in concrete. Strain gauges use the piezoelectric effect [18]. The change in length (strain) is converted to resistance change. The conducting wire is placed on a flexible material. If the length of the wire in the strain gauge is assumed to be L, the resistance R can be calculated as $R = \rho\frac{L}{A}$. Where ρ is the resistivity and A is the cross-sectional area of the wire [19]. The output of the strain gauge is interpreted using Wheatstone bridge, 2.16 such that the voltage output will be proportional to the resistance change.

The strain gauge may form one or more arms of the Wheatstone bridge. A strain gauge can detect local deformations and follows a tedious setup procedure.

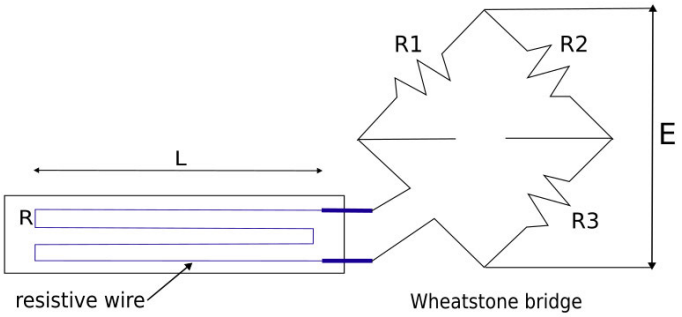

Figure 2.16: Working principle of a strain gauge

2. *Linear Variable Differential Transformer (LVDT):*
LVDTs utilise magnetic flux coupling for displacement measurement. It works on the principle of electromagnetic induction; LVDTs consist of stationary coils and a moving core. AC voltage is applied through the primary coil, which generates magnetic flux. A magnetic flux is generated due to the moving ferromagnetic core, and voltage is induced in the secondary coils [20, 21]. For SHM, LVDTs are used for measuring load vs displacement curves[22]. However, the LVDT can only measure local displacements. When placed between two points, the total change in distance is recorded.

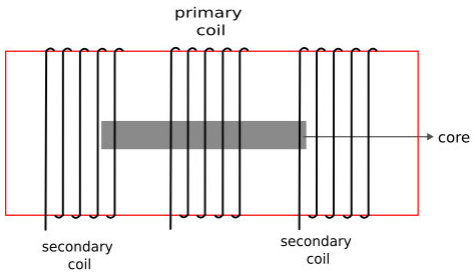

Figure 2.17: Working principle of LVDT

3. *Fiber optics:*
Fibre optics can be mounted or embedded in the concrete. If not embedded, small holes are drilled for installation [23]. The optical fibre cable forms the sensing and transmission part [24]. The phenomena of Total Internal Reflection form the basis of the fibre optics system. The light which gets reflected has a wavelength called Bragg's wavelength. Bragg's wavelength is related to the pitch and the refractive index, which are related to the strain and temperature.

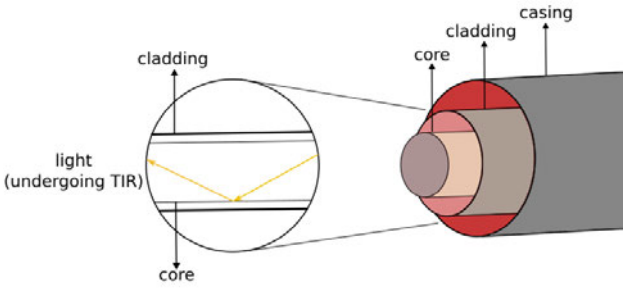

Figure 2.18: Working principle of fibre optics sensor

4. *Acoustic emission (AE):*
   On the onset of cracking, i.e., after a material (concrete) reaches the elastic limit, kinetic energy is released. This kinetic energy travels as waves and can be measured by surface sensors [25]. Micro cracks can be detected using AE. Crack types can be classified Based on the wave signal type and the trend of specific parameters. This is subjected to numerous studies as the occurrence of noise is expected [26, 27].

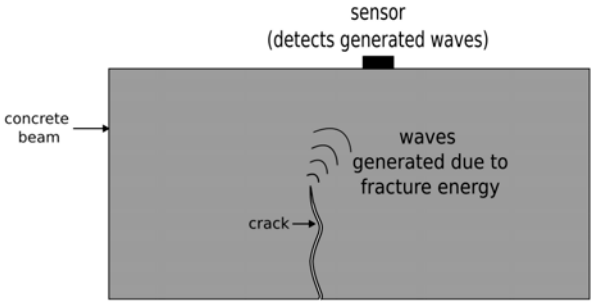

Figure 2.19: Working principle of acoustic emissions technique

5. *Digital Image Correlation:*
   DIC can check strain, stress and crack development (in-plane) in a concrete structure. It is a non-contact method and uses a sequence of images to identify deformation patterns [28]. The surface of the structure is covered in a granular pattern which is referred to as a speckle pattern. The pattern changes as deformation occurs. Using pixel packets, displacement in 2D, 3D and strain maps can be developed [29]. The images require post-processing causing delays in obtaining results. Limitations of this technique depend on the type of camera used and the speckle pattern.

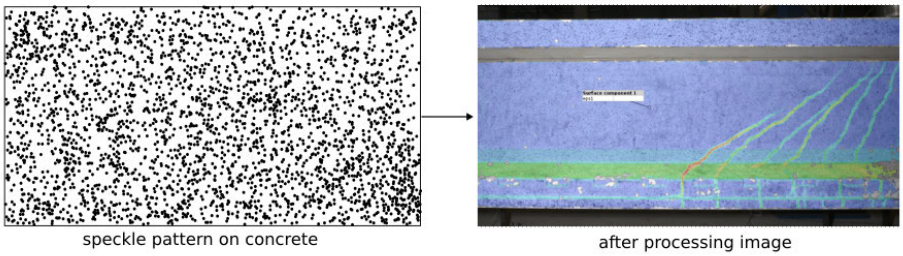

Figure 2.20: Working principle of digital Image Correlation

6. *Ground Penetrating Radar (GPR):*
   Another popular technique used on concrete structures like bridges is GPR. It is used for the determination of location of rebars in the concrete, moisture and chloride content as it leads to corrosion of the rebars. All materials have different electric permittivity, ϵ_r, and when electromagnetic (EM) pulses pass from one material to another, the EM pulses are reflected [30]. Concrete has a very low ϵ_r value and can be neglected. However, steel has an infinite net ϵ_r. Therefore, the EM pulses will be reflected from the reinforcement in the concrete structure. GPR equipment consists of a transmitter, a receiver and additional units for processing and display of evaluation [31].

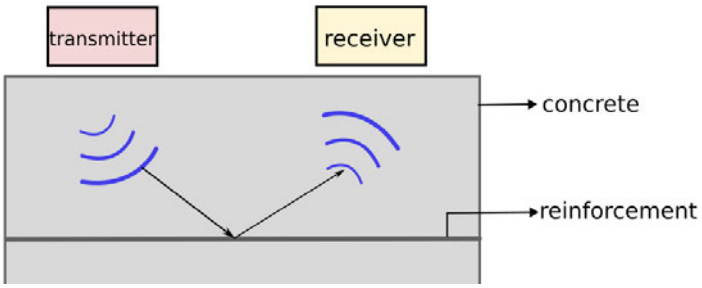

Figure 2.21: Working principle of ground penetrating radar

7. *Thermography:*
   Thermography or Infrared thermography (IRT) follows the Stefan-Boltzmann law. According to the law, the infrared radiations generated by a body is directly proportional to the T^4, where T is the temperature [32]. The concrete under inspection will heat up due to internal and external factors causing heat flux. Infrared cameras detect this heat flux, and thermograms are developed. Heat can be transferred to the concrete via natural heat sources like the sun or artificial heat source [33].

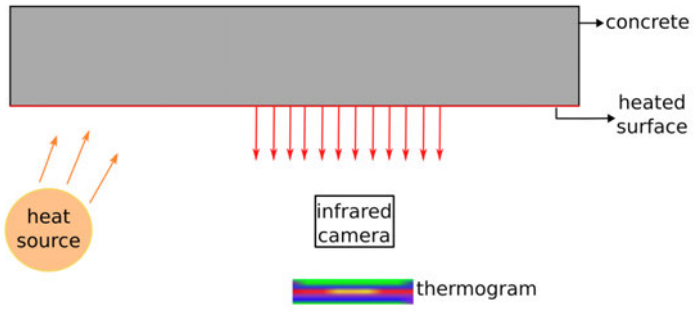

Figure 2.22: Working principle of thermography

8. *Ultrasonic Pulse Velocity (UPV):*
   Ultrasonic Pulse Velocity is another method which utilises elastic wave detection for concrete behaviour. Unlike in case of AE, an ultrasonic pulse is generated by a transducer for wave propagation. The components that make up the system consist of a transmitting transducer and receiving transducer. Elasto-acoustic waves are transmitted as mechanical waves which reflect due to phase change inside the concrete, and these reflected vibrations are collected as electric signals at the receiving side [34].

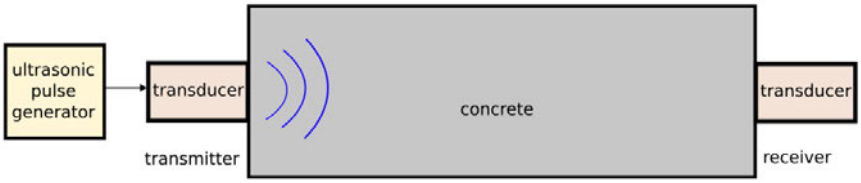

Figure 2.23: Working principle of ultraviolet Pulse Velocity

9. *Magnetic sensors:*
   Fluxgate magnetometer, Hall effect (HE) sensors, Magneto-resistive (MR) sensors, Eddy current testing (ECT), and SQUID sensors are commonly used magnetic sensors [35]. They work on different principles of the electromagnetic field. Magnetic sensors are most widely used to detect corrosion in the reinforcements and cracks in concrete. HE and MR sensors have found enormous scope in NDE for materials over other types of sensors [36, 37]. For the research in this study, AMR sensors are used for crack monitoring.

Technique	Working principle	Advantages	Disadvantages
Strain gauge	Based on the change in resistance due to mechanical strain.	High sensitivity towards strain/deformation measurements.	Susceptible to temperature and mechanical disturbances.
LVDT	Utilises electromagnetic induction by change in magnetic coupling.	High accuracy and linear relation between displacement and electrical output.	Electromagnetic interference can affect the accuracy.
Fibre op ics	Via total internal reflection, light signals are transmitted.	Long range transmission without signal degradation.	Vulnerable to physical damage, therefore, requiring careful handling.
Acoustic emissions	Based on the detection of high frequency sound waves generated due to fracture energy.	Provides real time monitoring and detection of damage.	Requires experienced and expert analyst and sophisticated analysis technique.
DIC	An optical technique which compares pixel-level changes between images.	Provides non contact and spatially resolved measurements.	Preparation of surface and contrasting patterns in the test specimen poses a challenging.
GPR	Reflected electromagnetic pulses carry information about composition.	Non-destructive analysis of substructure can be obtained.	Data quality and moisture content compromise accuracy and data quality.
Thermography	Detection of heat flux by developing thermogram using infrared cameras.	Offers real time thermal patterns for a large area.	Ambient temperature and air flow can affect interpretation of thermograms.
UPV	Measures travel time of transmitted ultrasonic pulse.	Delivers rapid and efficient information via NDE.	Accuracy is affected by irregularities due to concrete composition.

Table 2.1: Comparative Analysis: Working Principle, Advantages, and Disadvantages

This study proposes a novel idea for implementing AMR sensors for SHM. The compact size of the sensor enables monitoring of otherwise inaccessible areas. As a wireless system, on-site inspection is not necessary after installation, and real-time data can be acquired. The proposed monitoring system is economical, facilitating scalability and practicality. Multiple sensors can be deployed to provide a denser network for data analysis. Further details are discussed in the next chapter.

3

Anisotropic Magneto Resistivity (AMR)

3.1. Introduction to AMR sensors

Integrating magnetic sensors in NDT has become an increased area of academic research as it makes sensor design more efficient [38]. A ferromagnetic film is used instead of an electromagnet for optimisation [39]. Ferromagnetic material exhibits higher anisotropic magnetoresistive properties. Anisotropic properties, as the name suggests, are dependent on the direction. Ferromagnetic materials exhibit spintronics properties that form the basis of AMR sensors. Spin electronics or spin-orbit interaction refers to the physics of electron spin, which can be detected by its magnetic moment [40]. Therefore, the ferromagnetic film will have a direction of magnetisation defined as the magnetic moment per unit volume. The direction of magnetisation can control the spin. When current passes through the sensors, resistance develops due to the rotation of the magnetisation of the sensor, as shown in Figure 3.1.

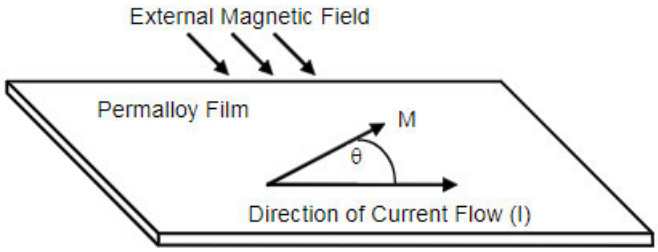

Figure 3.1: Working principle of AMR sensor

Anisotropic sensors are a type of magnetic sensor widely used. Sensors based on AMR can work with either the south pole or the north pole. This means it is not sensitive to polarity [41]. Consequently, the response from a positive field will be the same as from a negative field. Due to the resistance development, the sensors can achieve higher sensitivity. However, the sensor might measure the voltage offset or the DC magnetic field [42], which can cause a reduction in the

quality of performance. Therefore, AMR sensors are designed in the form of a Wheatstone bridge [43].

3.2. RedFox Villari-2 (RFV-2) monitoring system

The RFV-2 sensors are patented AMR sensors that measure the magnetic flux density and help monitor cracks in steel structures. Magnetic flux density is synonymous with the magnetic field. Implementing the sensors in concrete structures is challenging as concrete, unlike steel, does not contribute to the magnetic field.

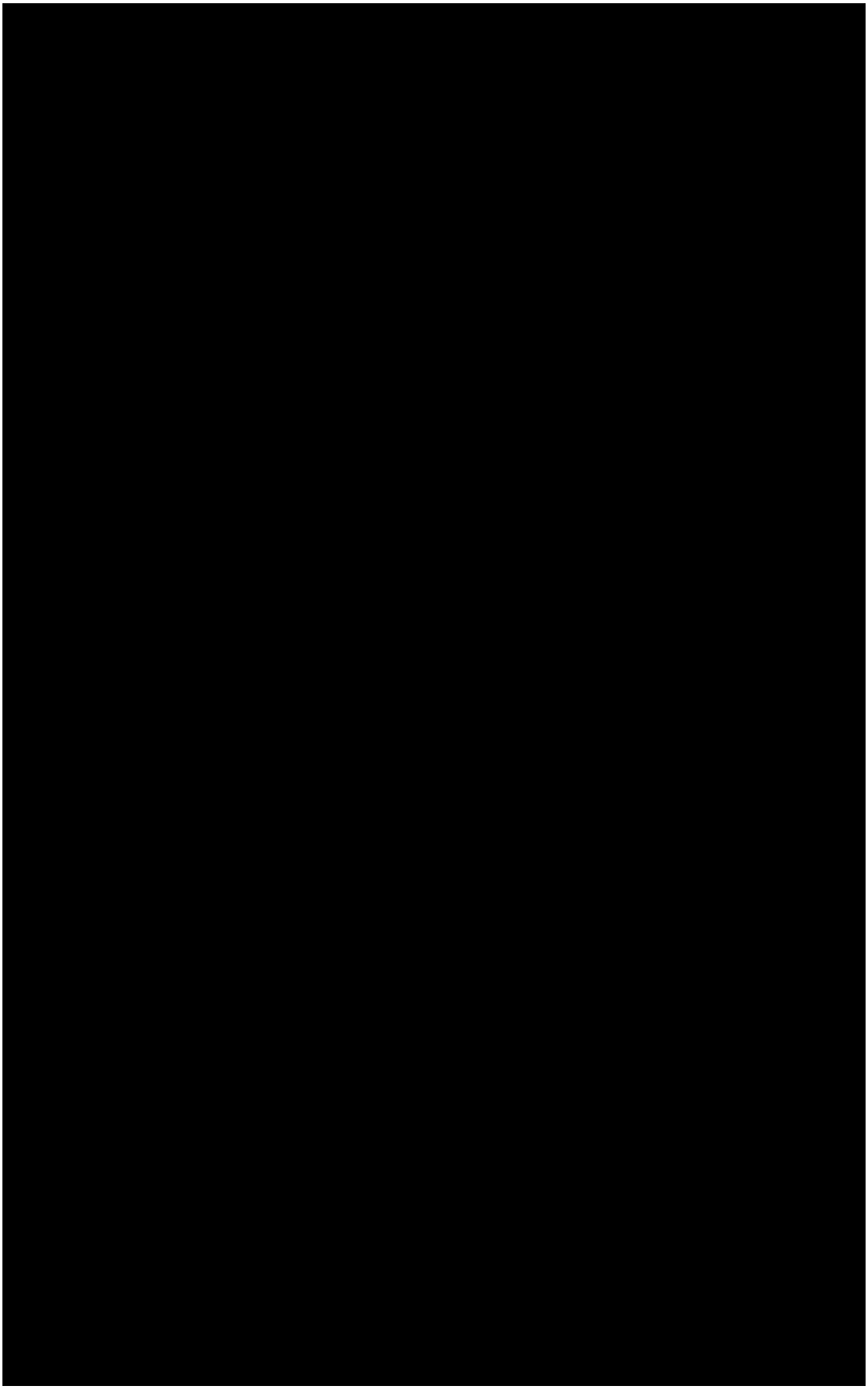

4

Magnetic field of a permanent magnet

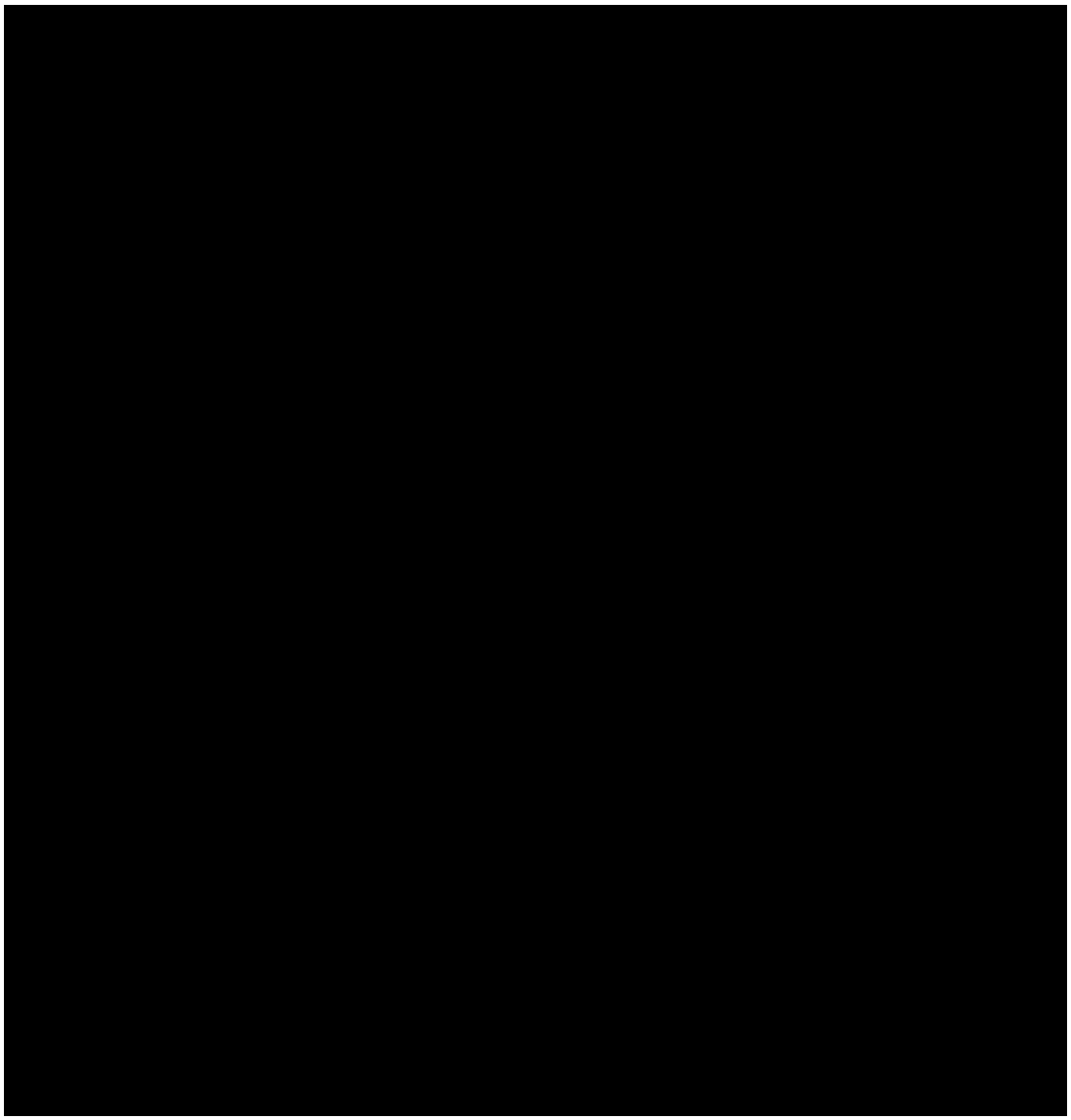

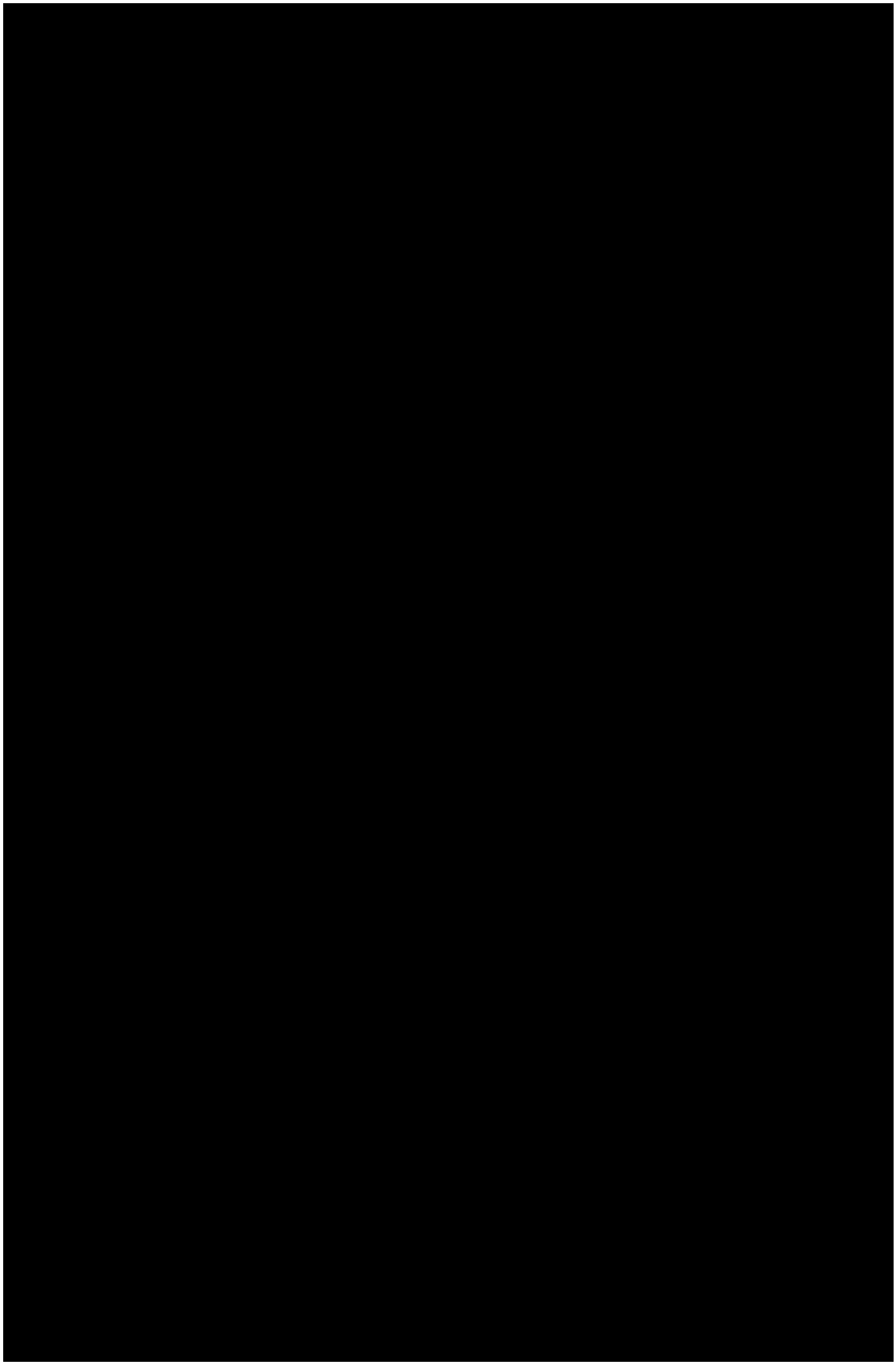

Material	Remnant flux density B_r(T)	Max working temperature (°C)	Curie Temperature (°C)
Neodymium	0.98-1.46	230	310
SmCo	0.74-1.17	350	825
Ferrite	0.2-0.43	400	450
Alnico	0.60-1.10	520	720

Table 4.1: Properties of permanent magnets

Magnet type	Ferrite	Alnico	SmCo	Neodymium (with coating)
Temperature resistance	High	Higher	Highest	Lower
Corrosion resistance	Highest	Higher	High	High
Coercivity	Lower	Higher	Highest	High
Strength	Lower	High	Higher	Highest
Economic value	Cost effective	Expensive	Most expensive	Expensive
Brittleness	Lower	Lower	High	High

Table 4.2: Comparison of various parameters of permanent magnet

4.1. Finite element model

It can be complicated to calculate the field distribution in a three-dimensional model as three components of the magnetic field B_x, B_y and B_z contribute to the total magnetic field; B_{total}. Therefore, finite element analysis is performed for neodymium magnets. On the basis of the finite element analysis, the most favourable setup is found for the experiments. For the finite element model, a disk magnet with radius $10mm$ and height $6mm$ are modelled at the origin 4.3. The background field is assumed to be 0 μT. The parameters used for the study are:

B = Magnetic flux density [T]
B_r = Remanent magnetic flux density [T]
H = Magnetic field strength [A/m]
μ_0 = Permeability [H/m]
μ_r = Relative permeability

The FEA is based on the following equations:

1. The first equation is based on Gauss's law of magnetism which states that the magnetic flux for any closed surface is always zero for the dipole source. It ensures that no additional source of magnetism occurs in the finite element domain.

$$\nabla \cdot B = 0 \tag{4.1}$$

2. The second equation is based on the relationship between magnetic flux density and magnetic field strength. It also accounts for the material property

by incorporating μ_r.

$$B = \mu_0 \mu_r H + B_r \tag{4.2}$$

3. The final equation is derived from Ampere's law. It states that the magnetic field strength is proportional to the current flowing in a closed space. Since, for the study, no currents are flowing, the curl of H will be zero.

$$H = -\nabla V_m \tag{4.3}$$

N38 grade neodymium magnet is modelled. Relative permeability, $\mu_r = 1.05$ for neodymium and the initial magnetic scalar potential $V_m = 0$. The net magnetic flux density inside the domain should remain zero, i.e., the magnetic flux density is conserved as described by the first Maxwell equation. The FE model uses the following constitutive law based on the direction of magnetisation,

$$B_r = \| B_r \| \frac{e}{\| e \|} \tag{4.4}$$

e is the direction of the remanent field or direction of magnetisation, which in this case is axially oriented. Therefore,

$$e = \begin{bmatrix} 0 \\ 0 \\ 1 \end{bmatrix}$$

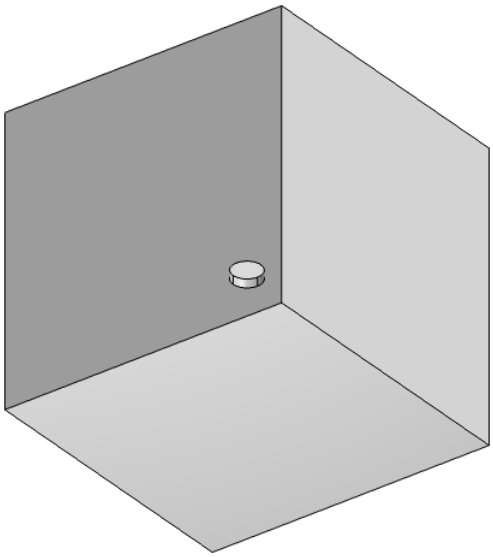

Figure 4.3: Finite element model of a disk magnet at origin

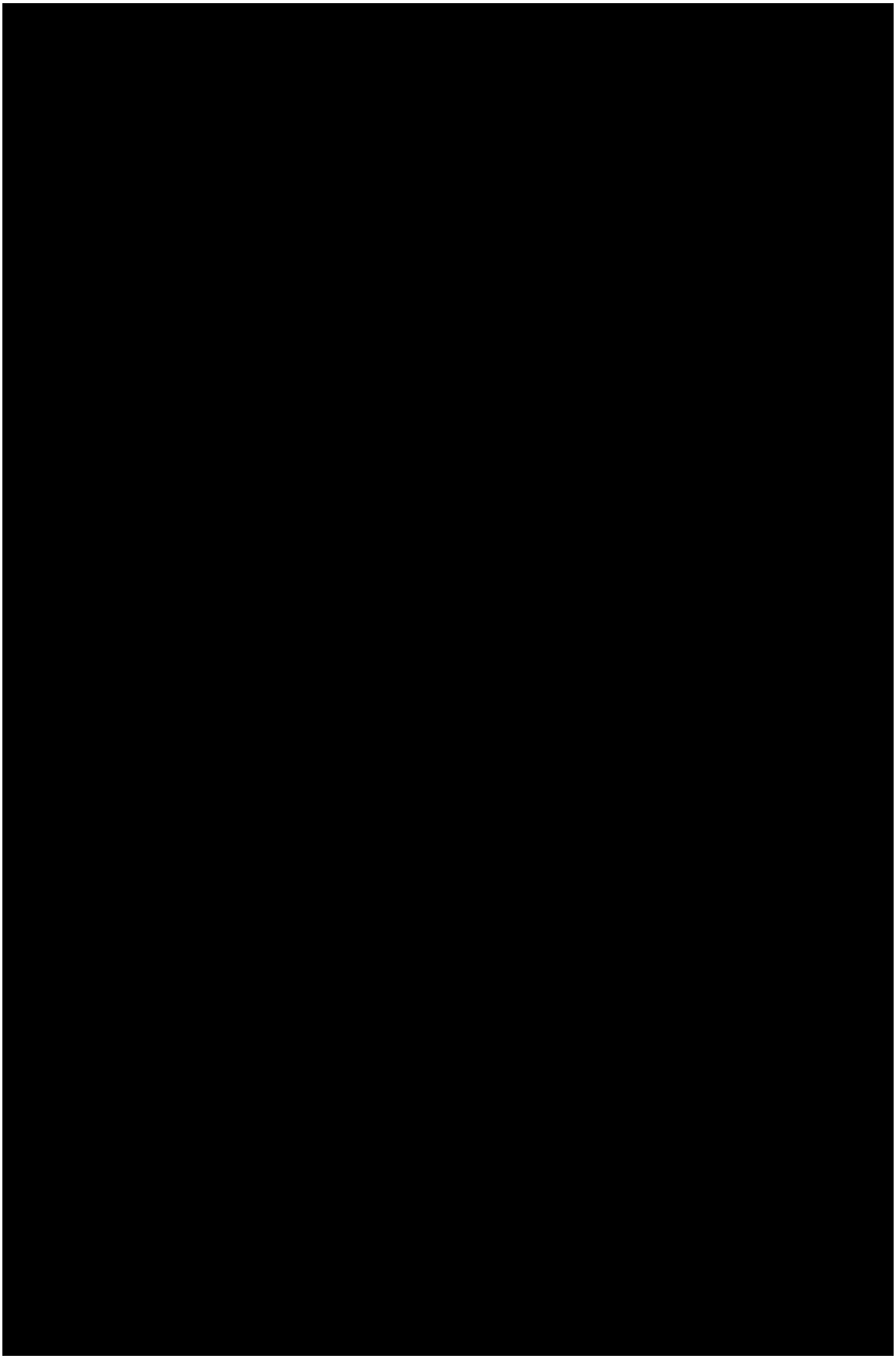

4.2. Analytical model for a disk magnet

Equations for a three-dimensional magnetic field are quite complex. Several studies have been performed to reduce the complexity for better applications of the equations. One approach suggested in [45] attributes a fictitious surface charge density (σ_M) to the magnet such that it is polarised in the z-direction (axial). The polarization, $M(\vec{z})$ can be formulated as:

$$\begin{aligned} M(\vec{z}) &= M \cdot \hat{z} \\ \sigma_M &= M \cdot \hat{n} \end{aligned} \tag{4.5}$$

$\hat{n}$ is a unit vector and is normal to the surface.

In [46] a coulombian approach for approximation of the magnetic field is described where the disk magnet of diameter $20mm$ and height $6mm$ is divided into N rectangular elements. The sum of the magnetic field of all elements will result in the total field of the magnet. For a 3D model, three components of the magnetic field are calculated using the formulas,

$$\begin{aligned} B_x &= \frac{J}{\mu_0} \sum_{e=1}^{N} \sum_{i=0}^{1} \sum_{j=0}^{1} \sum_{k=0}^{1} (-1)^{i+j+k} log(R_e - U_e) \\ B_y &= \frac{J}{\mu_0} \sum_{e=1}^{N} \sum_{i=0}^{1} \sum_{j=0}^{1} \sum_{k=0}^{1} (-1)^{i+j+k} log(R_e - V_e) \\ B_z &= \frac{J}{\mu_0} \sum_{e=1}^{N} \sum_{i=0}^{1} \sum_{j=0}^{1} \sum_{k=0}^{1} (-1)^{i+j+k} arctan \frac{U_e V_e}{R_e W_e} \\ B_{total} &= \sqrt{{B_x}^2 + {B_y}^2 + {B_z}^2} \end{aligned} \tag{4.6}$$

To calculate the parameters U_e, V_e, W_e and R_e, the dimension of each element from 1 to N will be determined using the following equations based on the figure 4.6:

$$\begin{aligned} a &= \frac{r/2}{N} \\ \theta &= \frac{2e}{N}; e = 1, 2..N \\ b &= 2sin(\theta) \cdot r \\ h_x &= e \cdot a + \frac{a}{2} \end{aligned} \tag{4.7}$$

The observation points are located on a line such that the endpoints are $(\alpha, \beta, \gamma) = (10, 0, 0)$ and $(30, 0, 0)$ as shown in the figure 4.6.

$$\begin{aligned} U_e &= (\alpha - h_x) - (-1)^i a \\ V_e &= (\beta - h_y) - (-1)^j b \\ W_e &= (\gamma - h_z) - (-1)^k c \\ R_e &= \sqrt{{U_e}^2 + {V_e}^2 + {W_e}^2} \end{aligned} \tag{4.8}$$

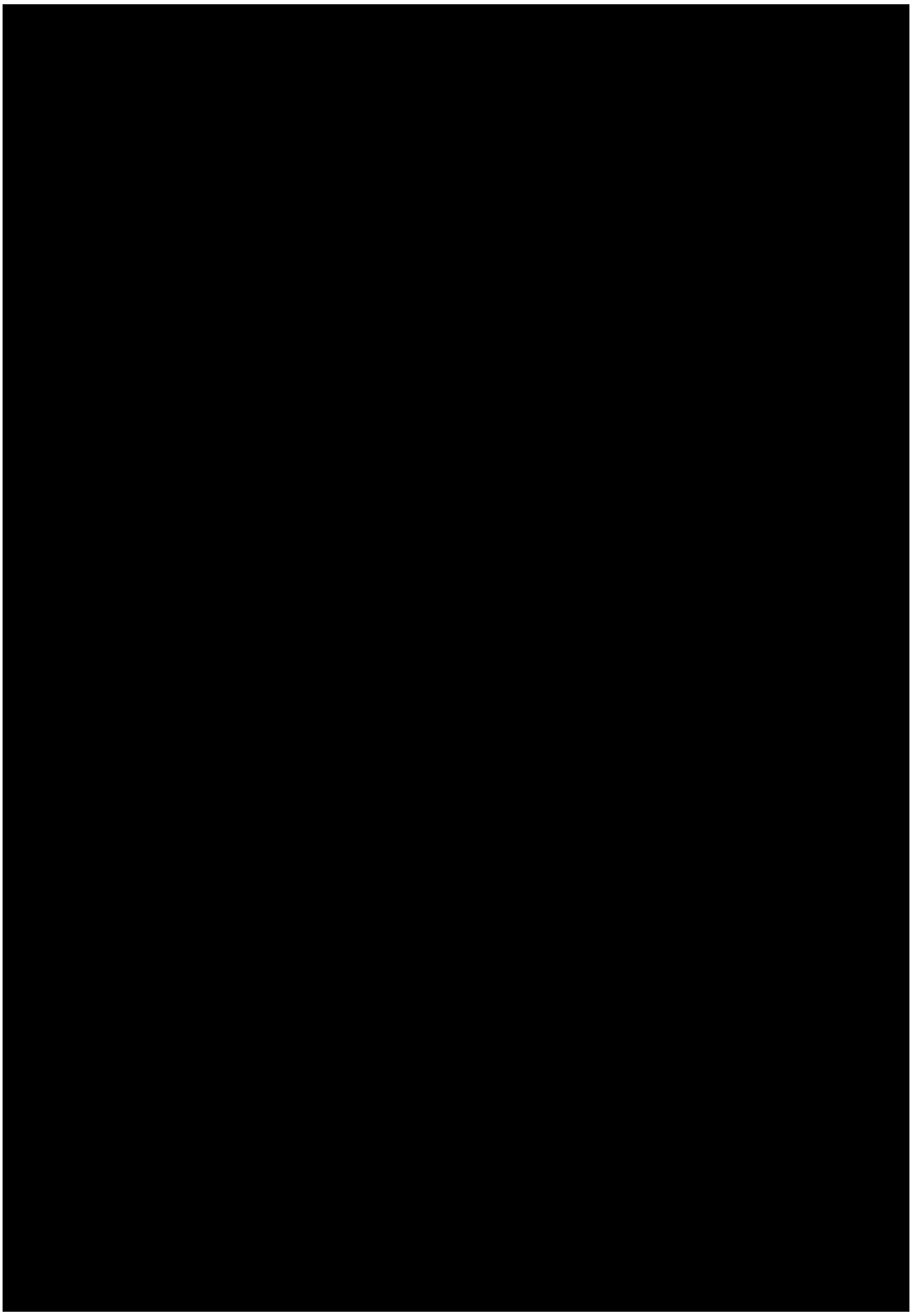

5

Conceptual validation of RFV-2 monitoring system

5.1. Overview of experimental model

Concrete crack monitoring has increasingly become a necessary field of study since concrete, a brittle material, is susceptible to cracking. Concrete cracks are prevalent. During the design phase, calculations are made for the crack width allowance for a safer design for the structure. However, new cracks can develop due to varying temperatures, humidity, loading conditions, and reactions within the concrete. These cracks propagate and become major cracks causing significant risk to the structure. Hence, a compact crack monitoring system that has an easy application on concrete surfaces and is economical is an essential tool for monitoring. The study focuses on developing a system for monitoring cracks under service conditions.

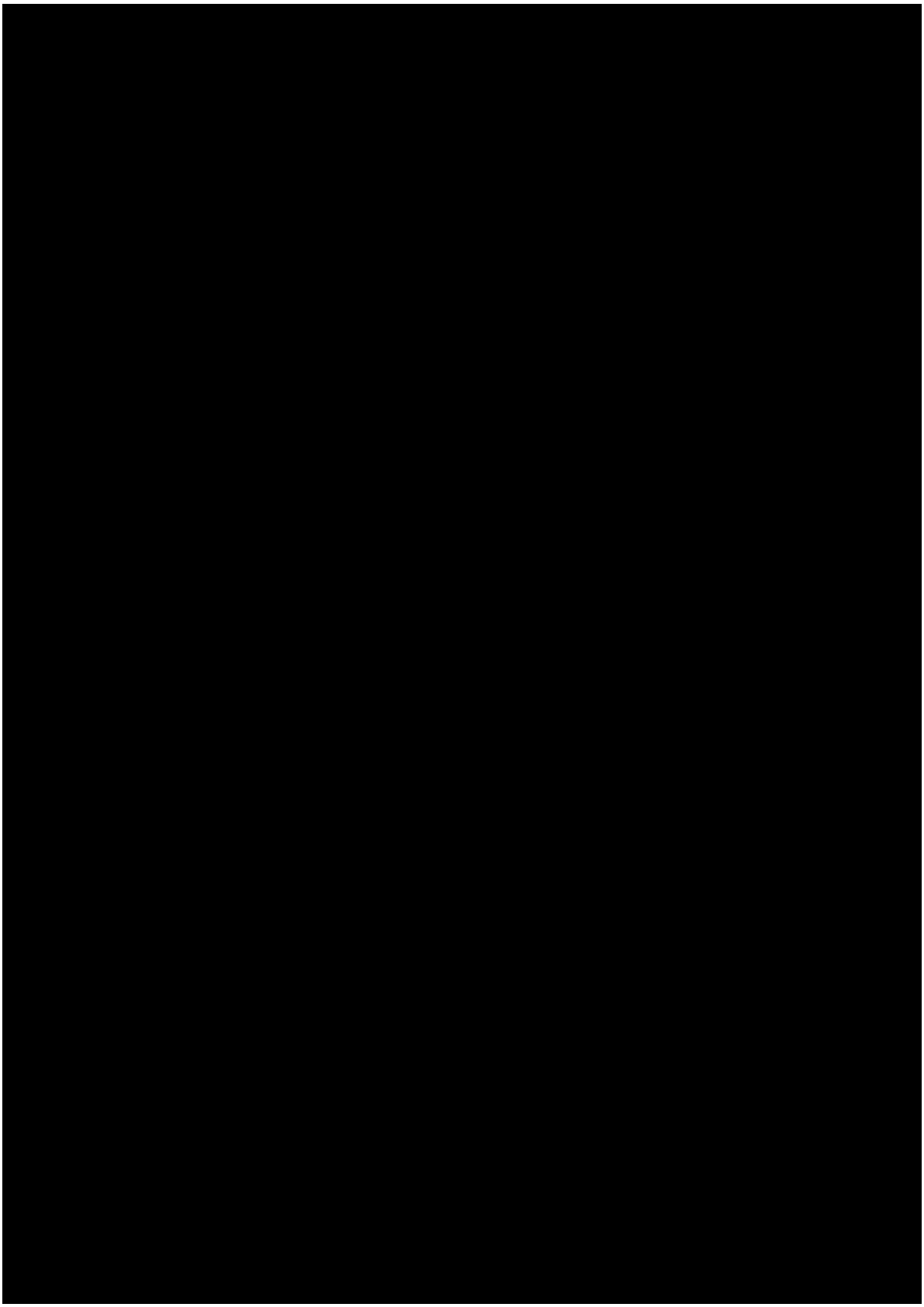

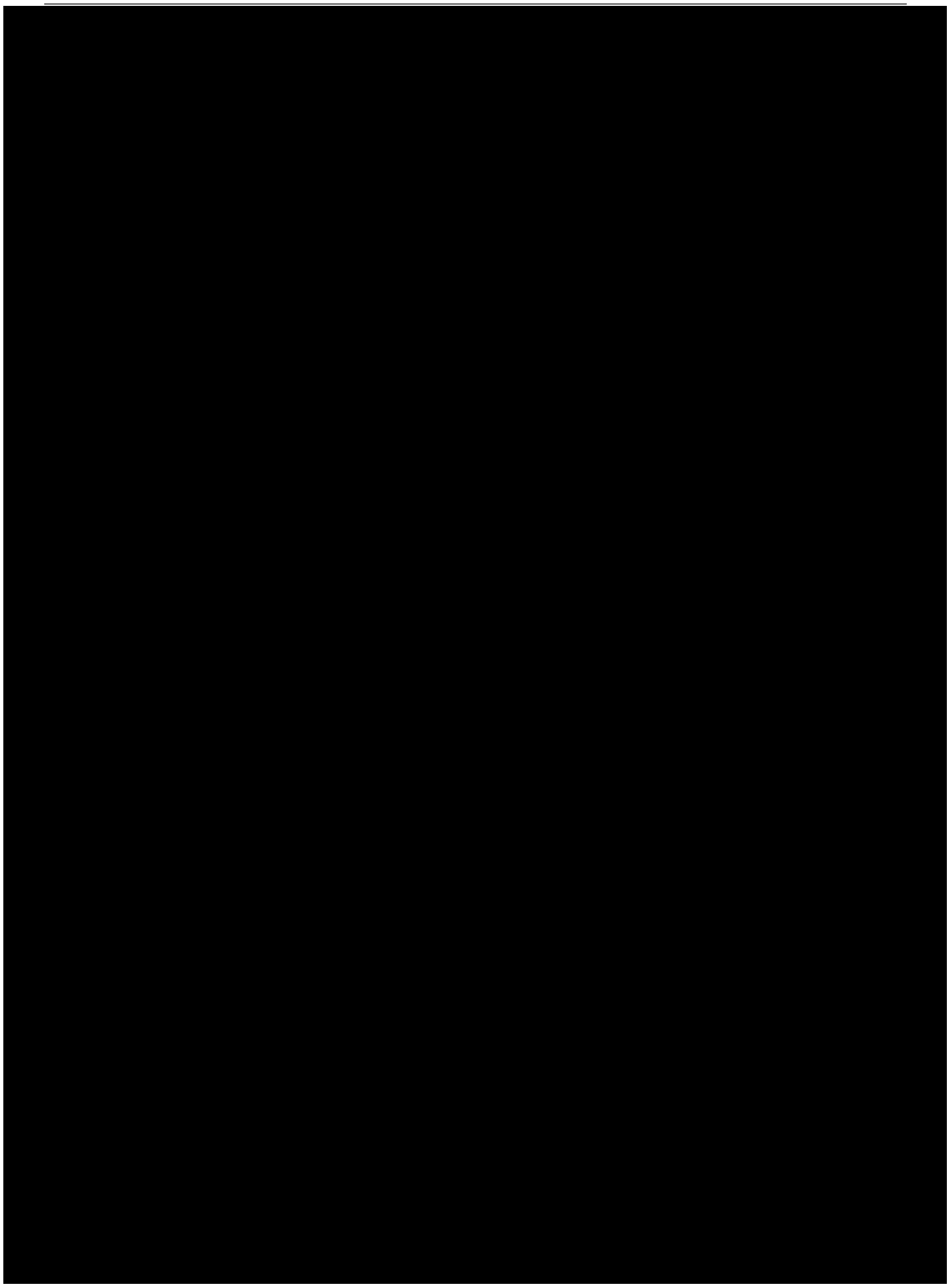

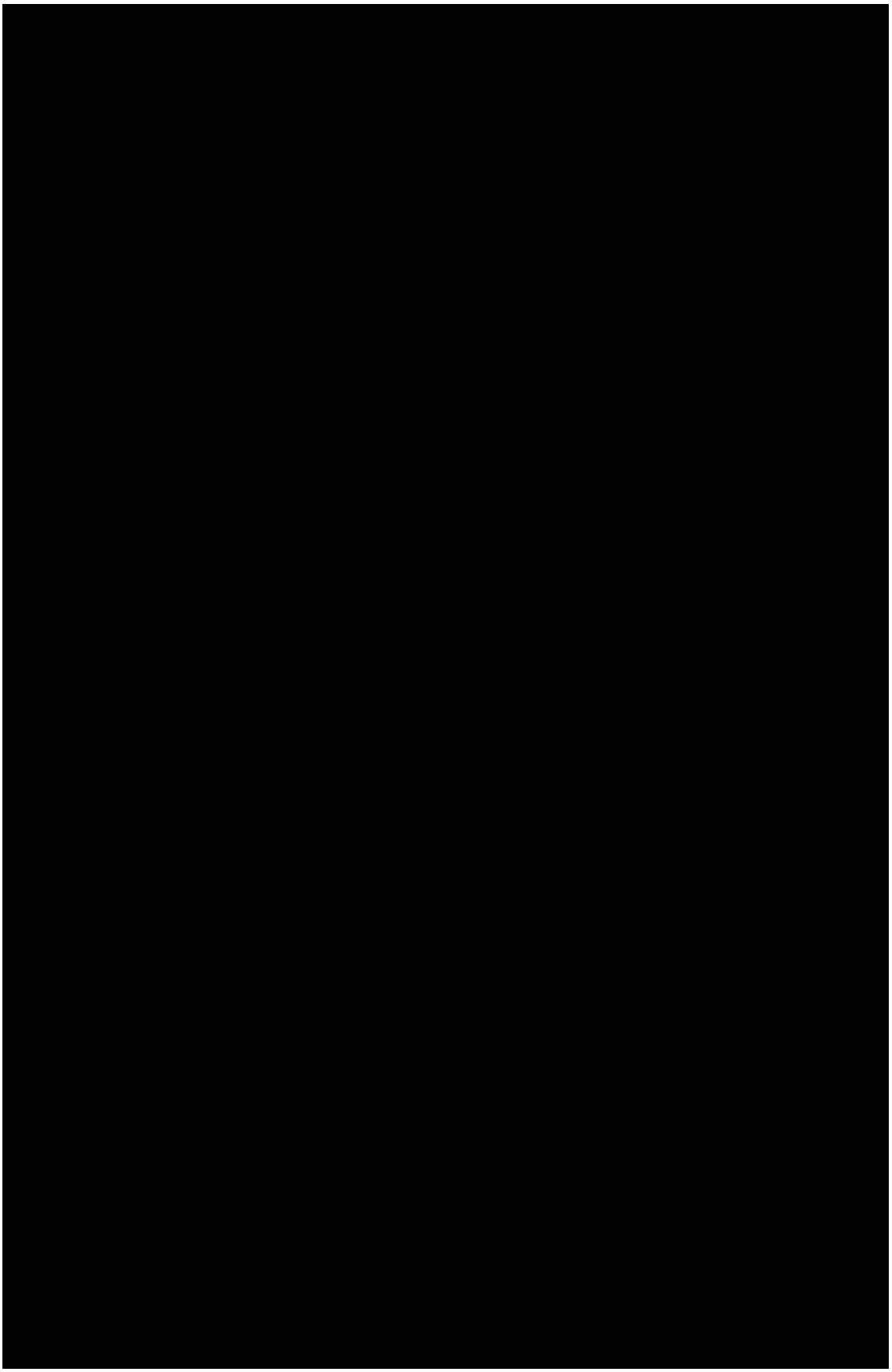

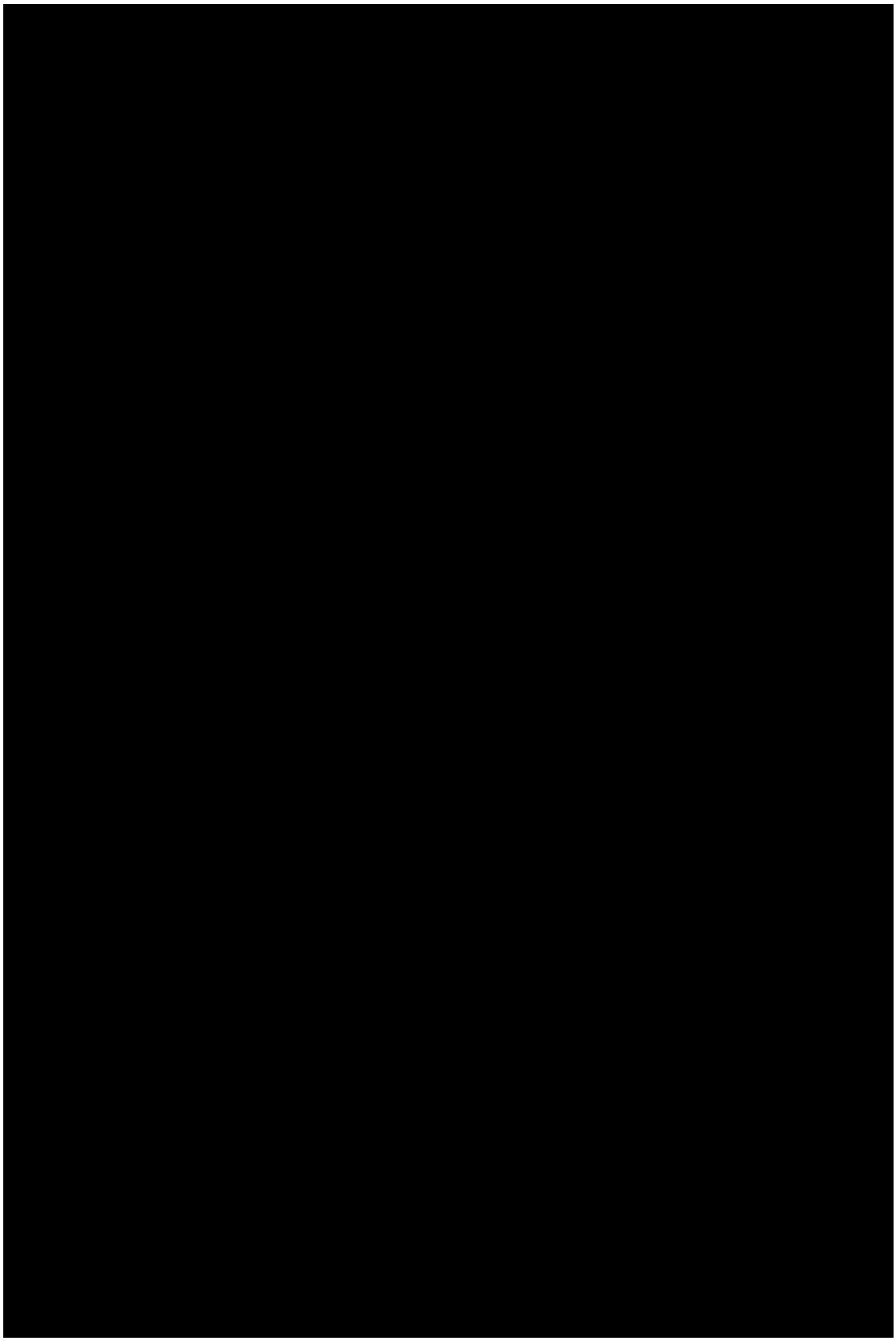

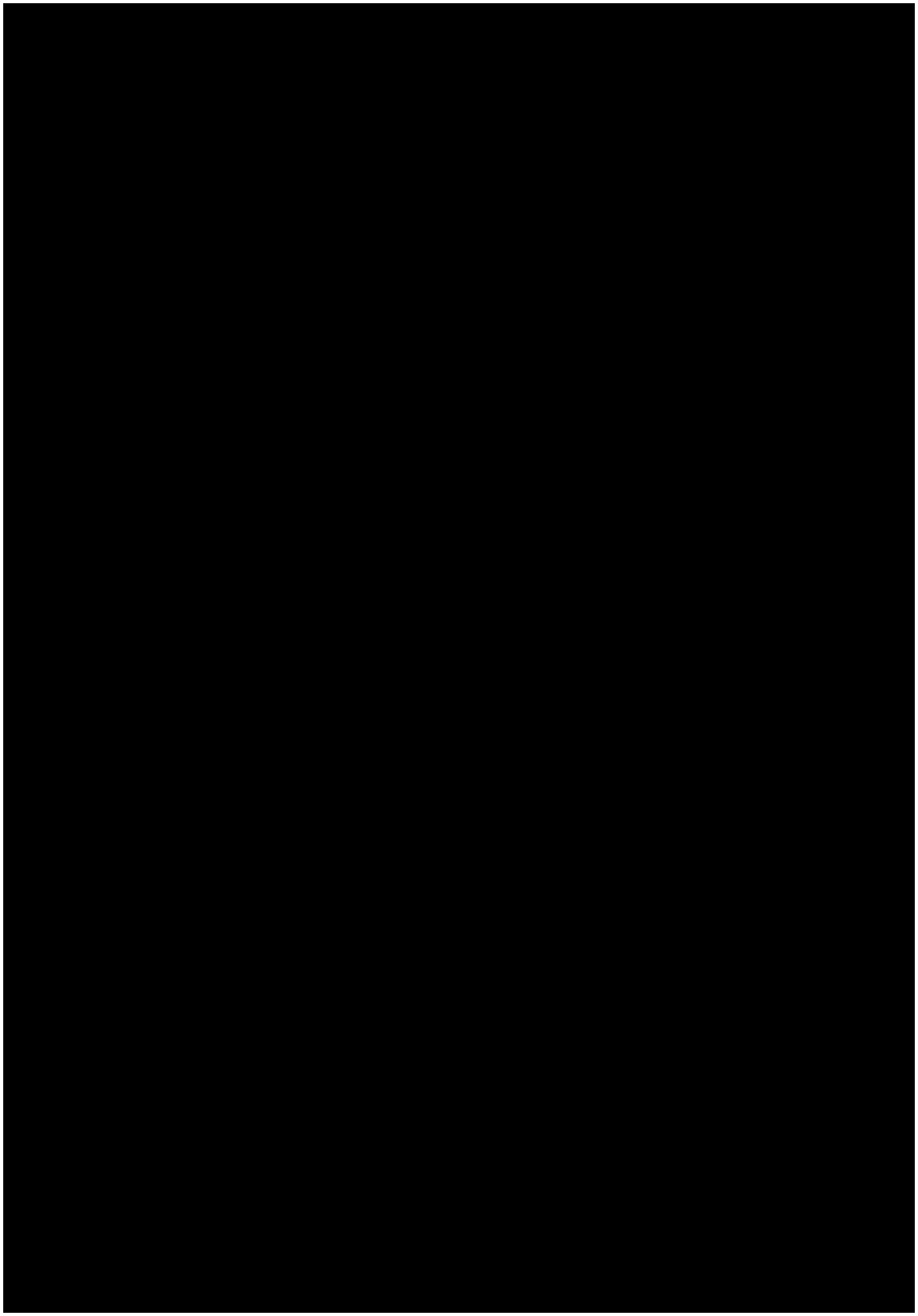

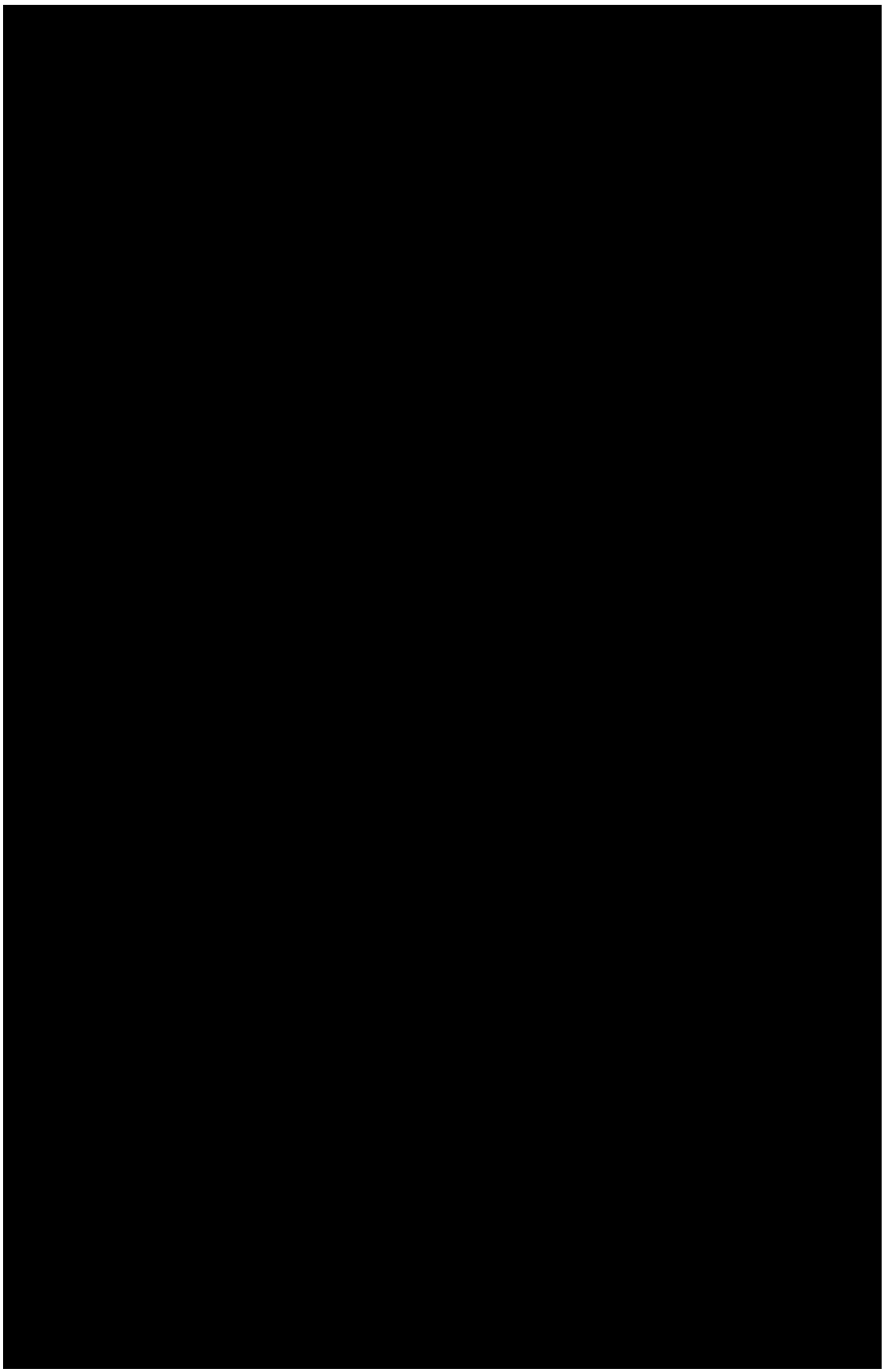

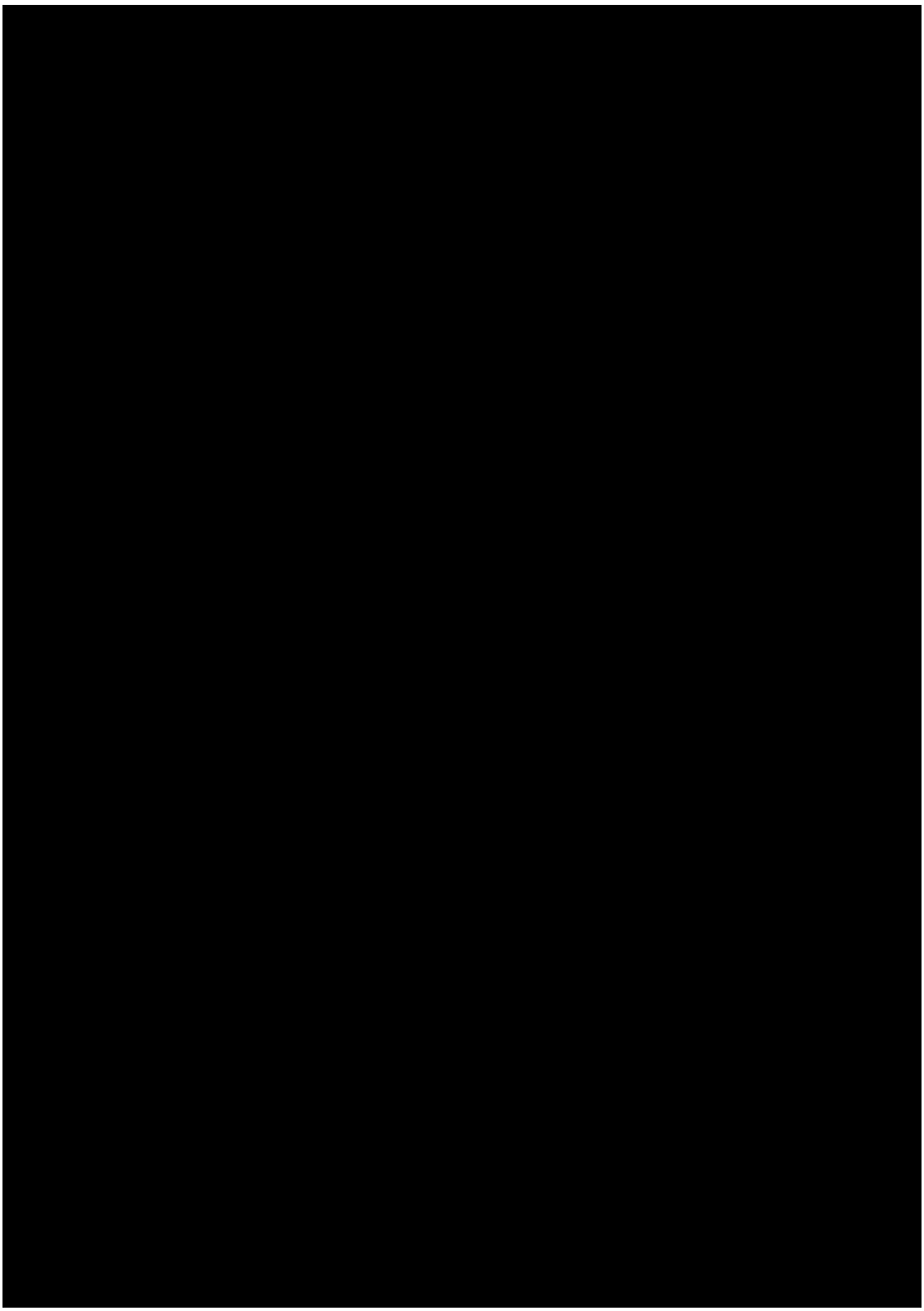

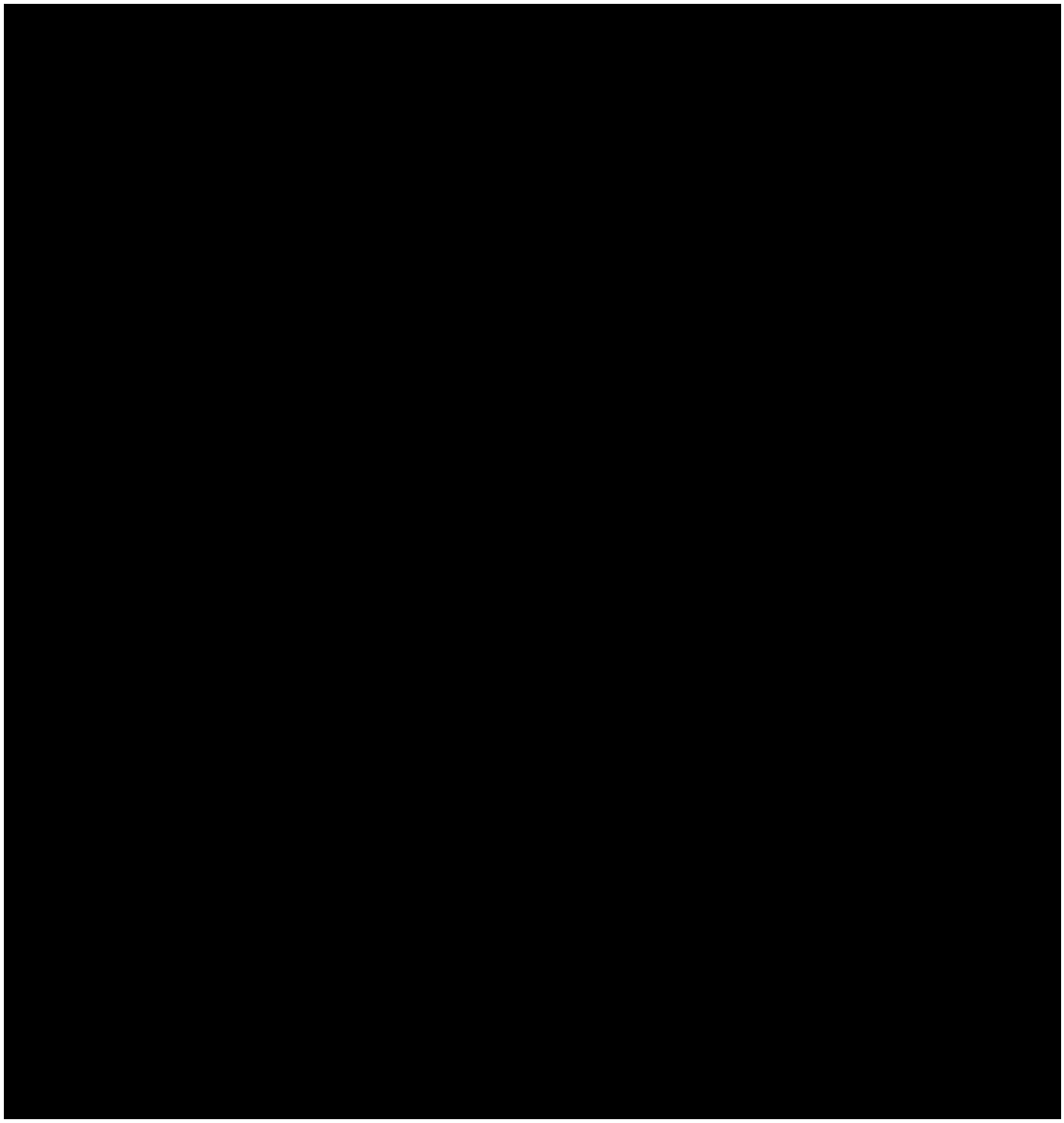

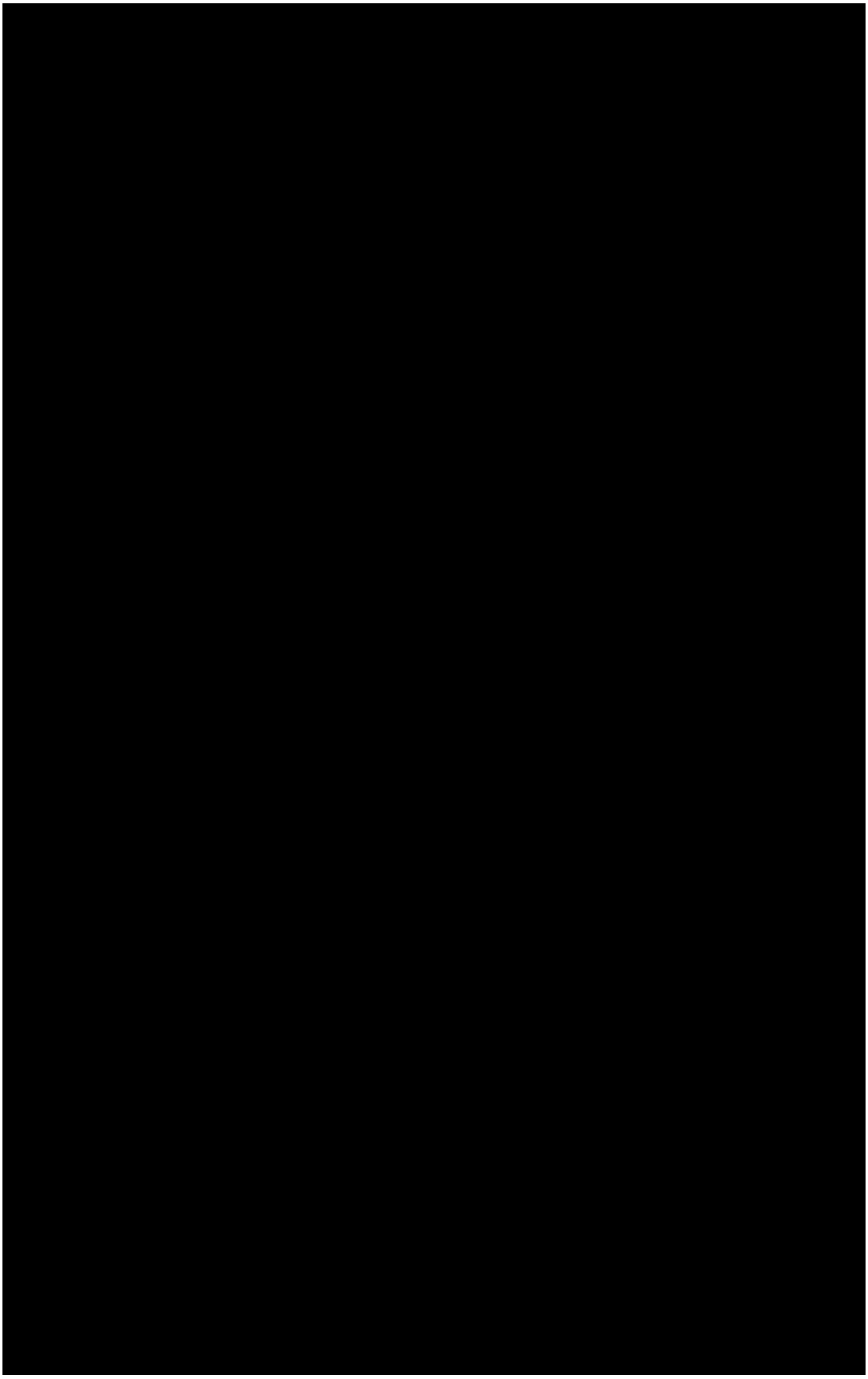

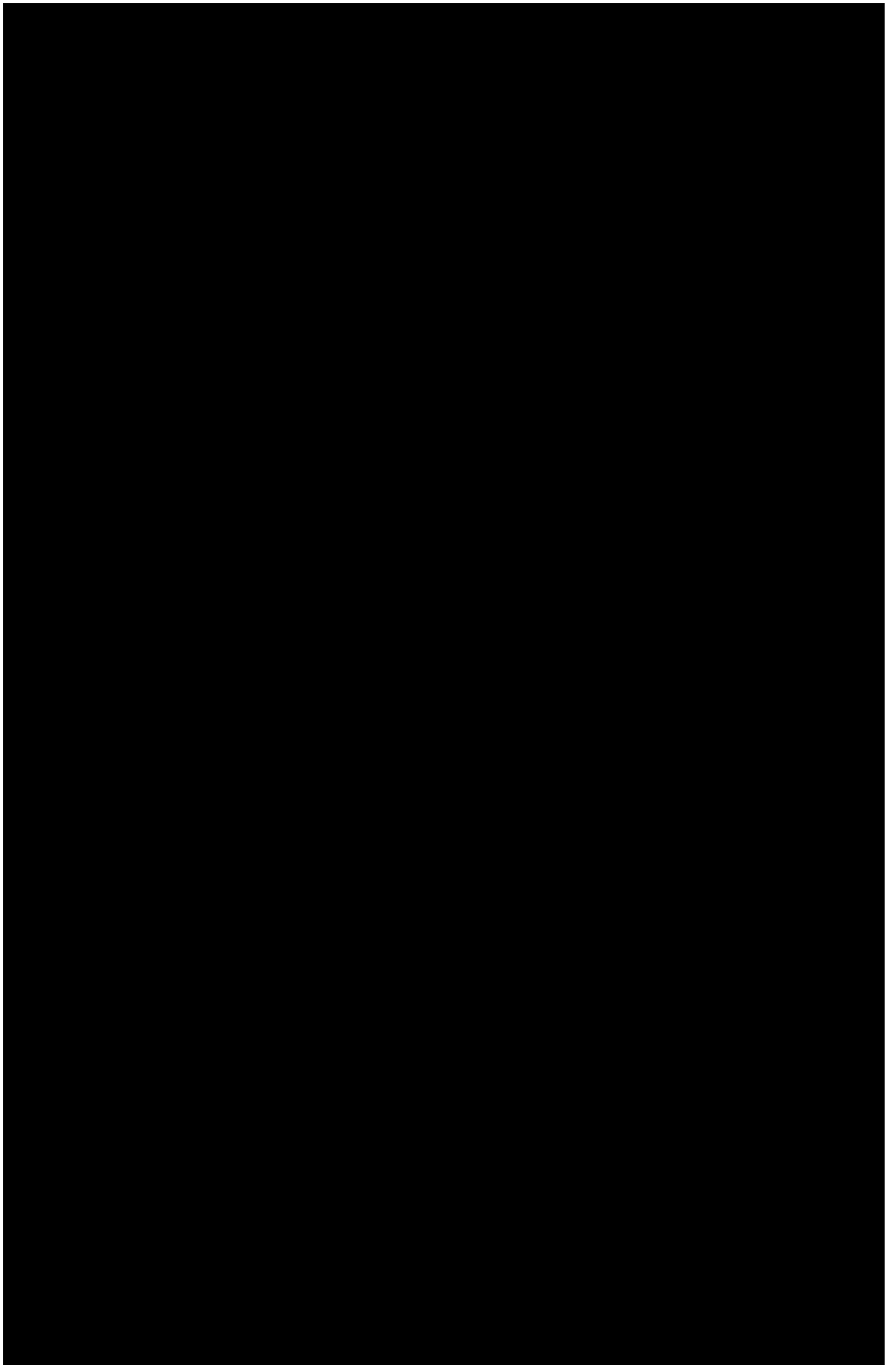

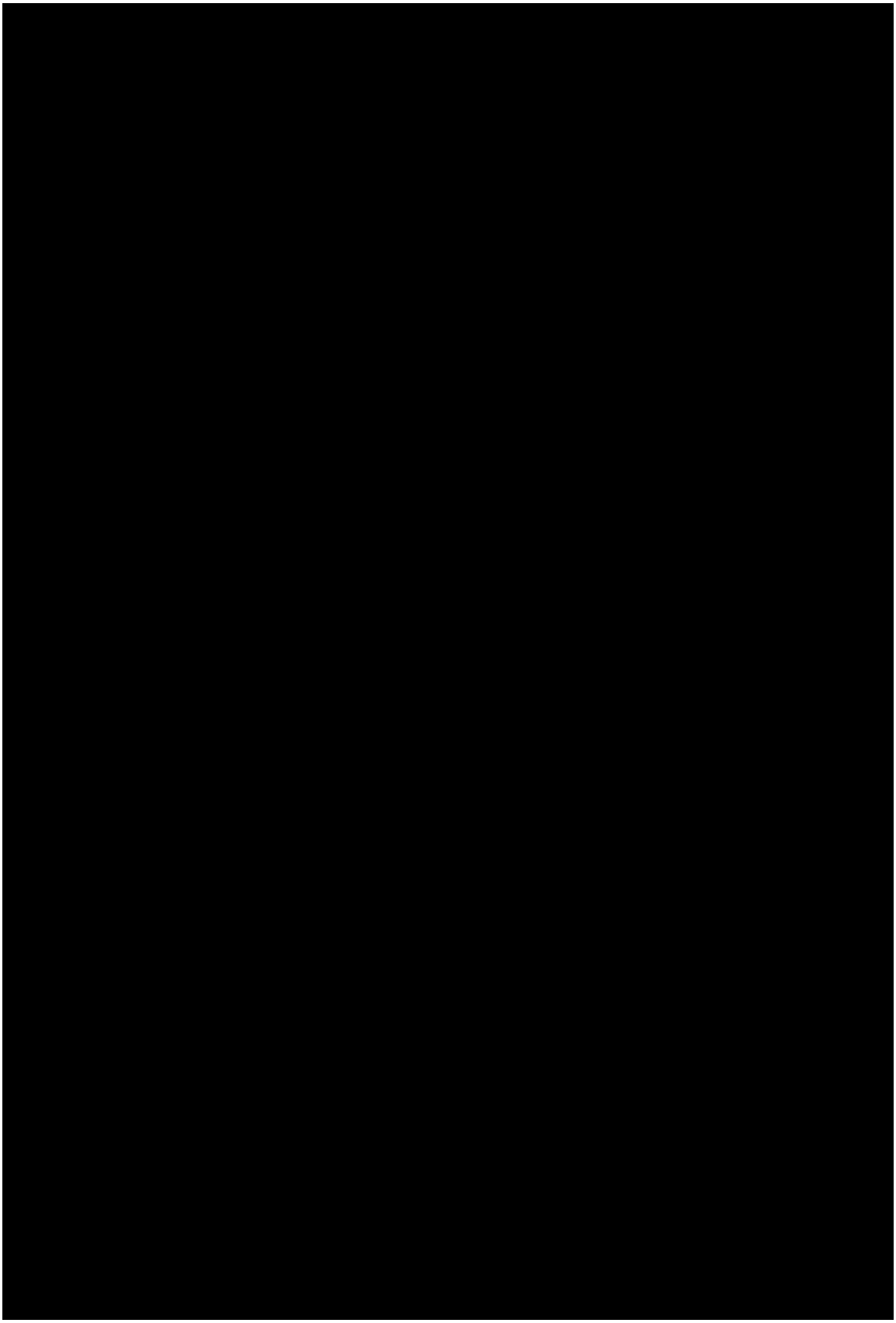

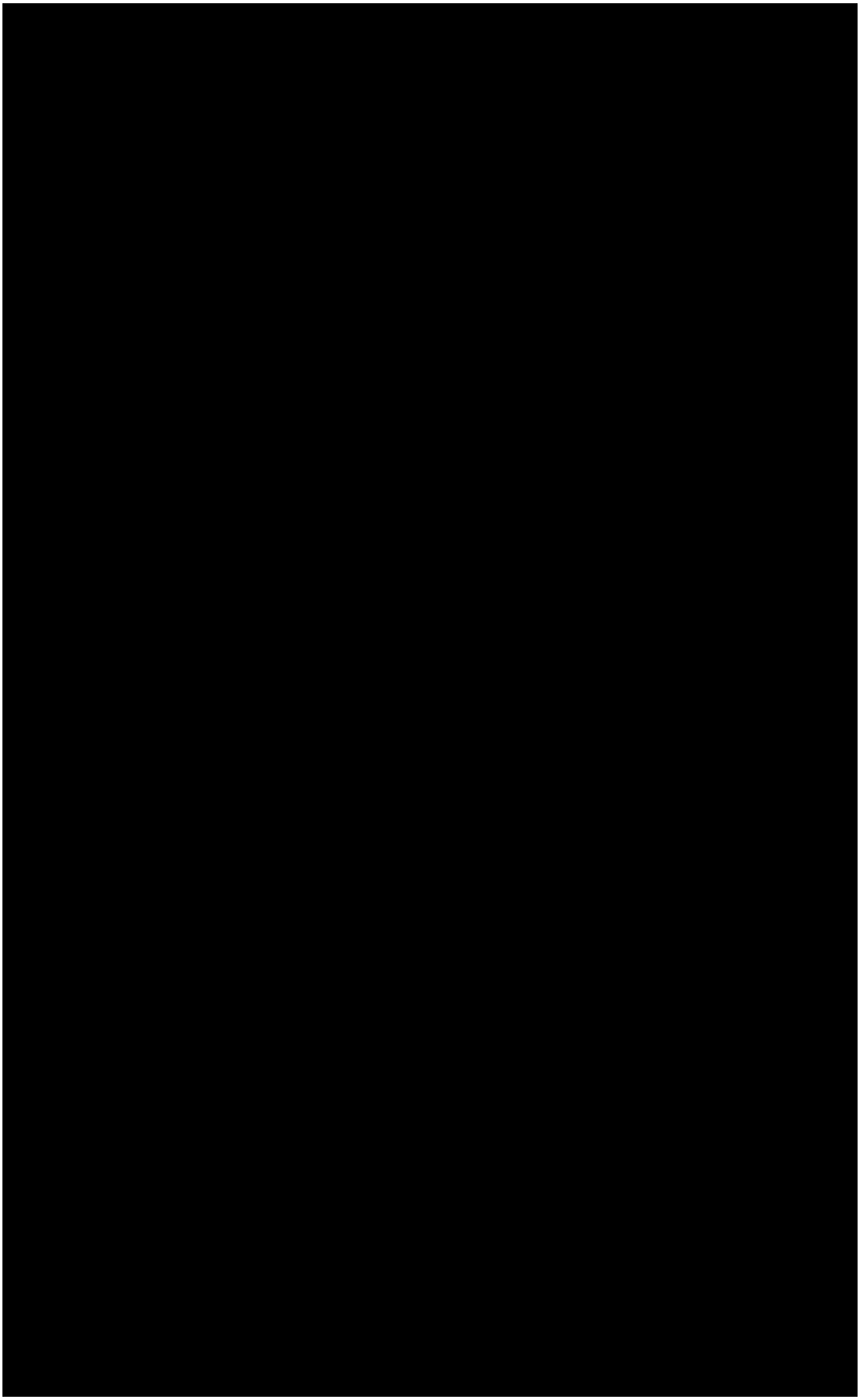

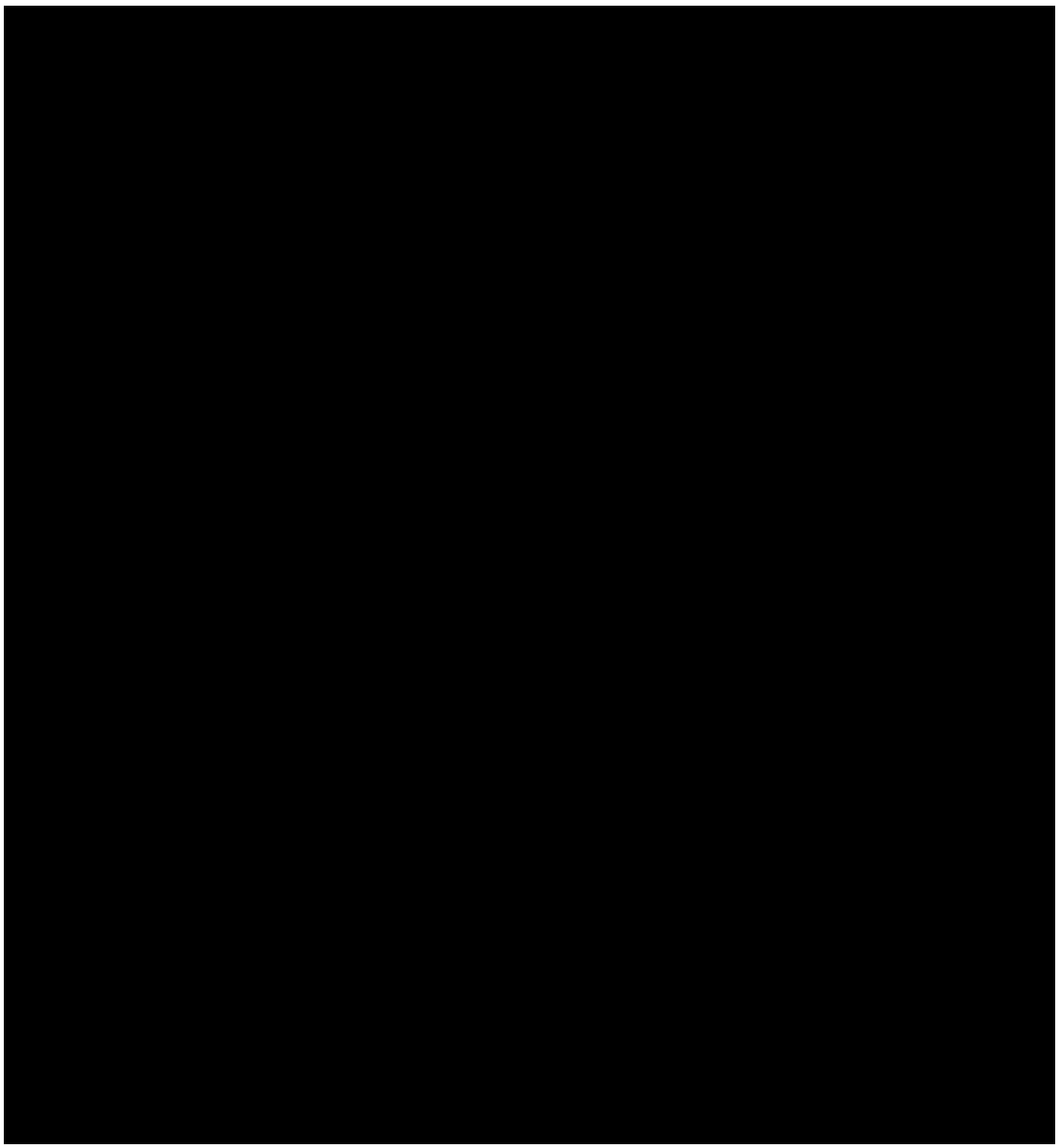

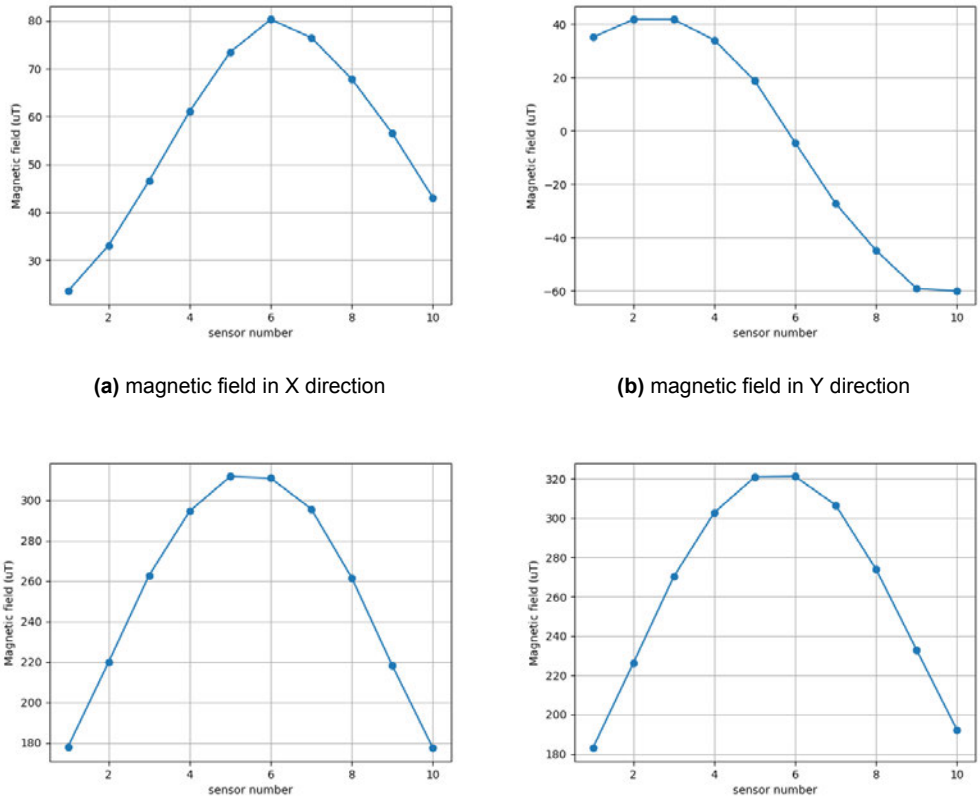

(a) magnetic field in X direction

(b) magnetic field in Y direction

(c) magnetic field in Z direction

(d) Total magnetic field

Figure 5.20: Magnetic field along sensor strip

5.4.1. Background field

There are several assumptions made in setting up the monitoring system. The magnetic field of Earth is fixed for a given location. It ranges from 25 to 65 μT on the surface. The RFV-2 is used to measure the background field. This background field will also include additional materials affecting the magnetic field. Since the experimental setup is designed to reduce the influence of extra materials affecting the field, the highest contribution to the background field comes from Earth's background field. According to [47], the magnetic field measured in delft is about 49.316 μT.

Sensor	X(μT)	Y(μT)	Z (μT)	B(μ)T)
1	39.40	13.04	40.85	58.60
2	42.84	0.28	42.07	60.05
3	29.54	-11.13	44.05	54.20
4	24.74	-12.16	42.95	51.04
5	24.17	-19.80	42.19	52.51
6	22.18	-3.780	42.43	47.97
7	26.16	9.50	41.15	49.68
8	28.00	3.09	42.59	51.07
9	25.47	-2.35	43.50	50.47
10	22.96	19.31	42.54	52.05

Table 5.2: Average background field

Since the magnetisation field on the sensor strip depends on the placement of various elements, as discussed earlier in the chapter, each sensor has a unique magnetic field. Therefore, each sensor's magnetic field is recorded and considered individually. The background field is measured for every step in the experiment, and it is concluded that the background field does not vary significantly. The average value of the background field is therefore considered for the experiments. Small displacements are simulated to replicate micro-cracking leading up to a crack of approximately 0.7 mm using the moving table. According to the Eurocode, the allowable crack sizes were limited to 0.4mm. Inspiration for the maximum crack widths was drawn from the maximum allowable values, and by taking advantage of the least count (1 μm) of the moving table, a continuous crack growth was replicated. Figure 5.21 shows the magnetic field components and the total field results from this experiment. The results are comparable to those from the manual moving table experiments. The nature of the graph follows the inverse square law A repeatability experiment is performed using the automatic moving table To check the consistency of the results. Figure 5.22 shows the results with a mean average error of 0.29%. The average error rate is calculated by first finding the error rate for each trial with respect to the first trial. The error rate found from each trial is then averaged out for the resultant error rate.

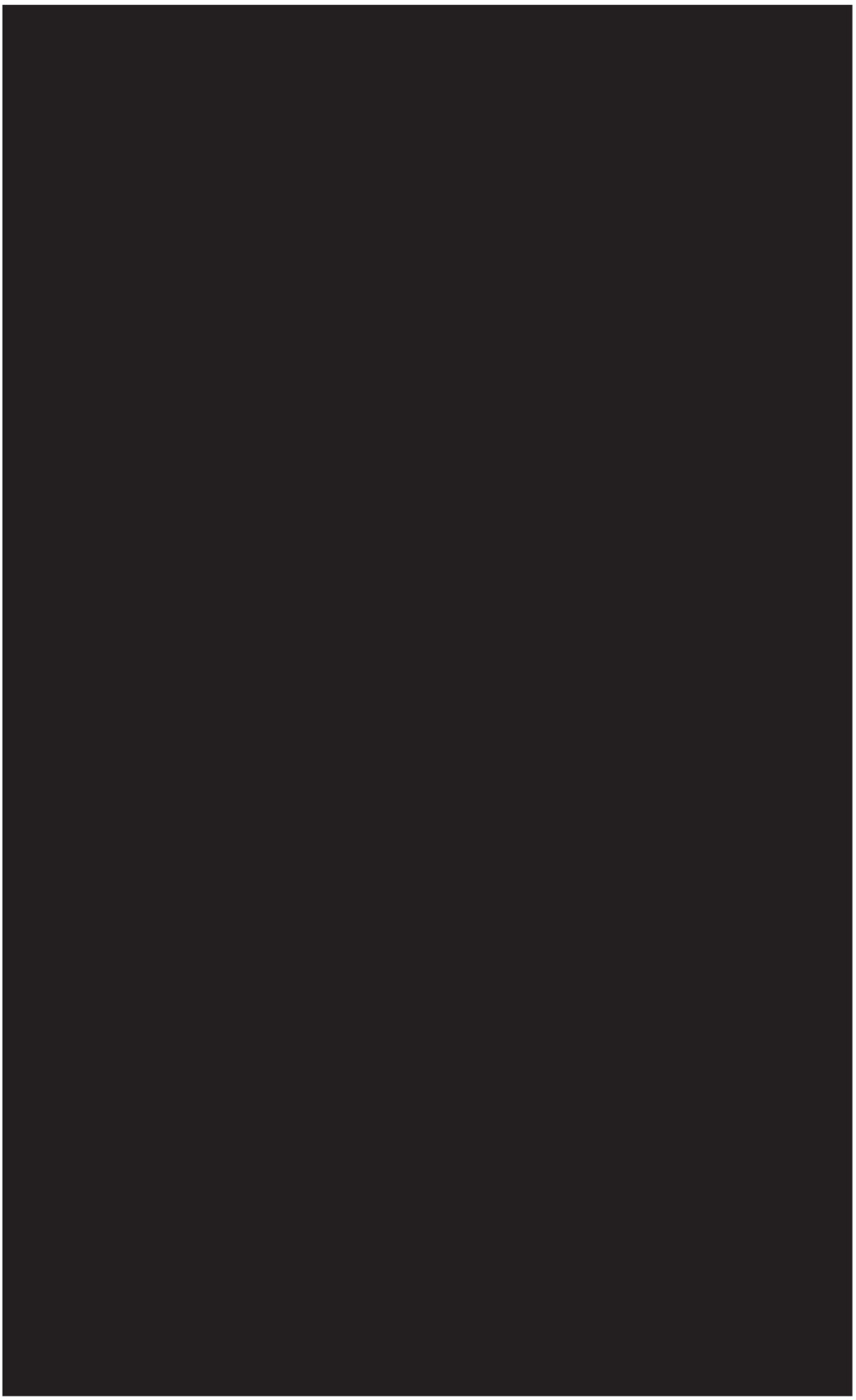

6

Four-point bending test

6.1. Four-point bending test

It is first assumed that the behaviour of the magnetic field should stay consistent with the results obtained in previous sections. However, due to the introduction of concrete in the setup, the material's behaviour should intervene, and a linear increase in the distance between the magnet and sensor strip is not expected. Based on the nature of the changes in the magnetic field described in section 5.3 and section 5.4, it is expected that the magnetic field will also exhibit variations in response to elastic deformation, as well as an increase in crack width. Before discussing the results, it is fundamental to understand the setup and the assumptions made. A four-point bending test is performed on the concrete prisms, chosen for their simplicity in crack type and ease of predicting the cracking region.

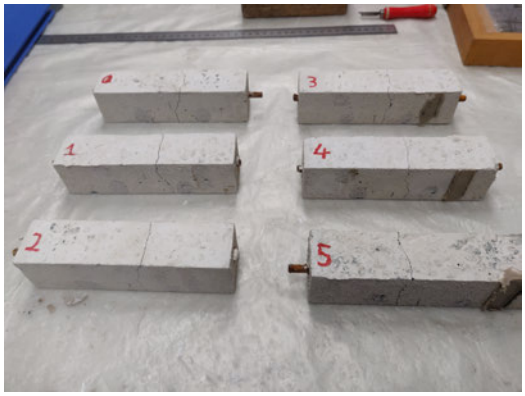

Figure 6.1: Cracked concrete prisms used for the test

Six samples are tested in this experiment, numbered from 0 to 5. Sample 0 is used as a reference to test the correctness of the procedure. Samples 1-4 are used for collecting data from the sensors (the types of sensors used are described in section 6.1.1). Sample number 5 measures the background field and evaluates other parameters that might affect the magnetic field.

6.1.1. Materials and dimension of concrete prisms

Concrete specimen of size 160mm x 40mm x 40mm is cast with a reinforcement of diameter 6mm. Grade C20/25 concrete is manufactured with a water-cement ratio of 0.5. Cement type CEM III/B is used, and the maximum aggregate size is 8mm. All specimens are cast from the same concrete batch. The 28-day compressive strength of concrete is 49.47 MPa. A smaller prism size is chosen for the experiment, as a smaller cracking region is required. Since the distance between the sensor strip and magnet can only be a few centimetres, a small-sized concrete bar is used. The reinforcement bar is placed so that the prism develops a single crack. The use of reinforcement will ensure that no brittle failure takes place. In a four-point bending test, a crack occurs due to bending, which causes the concrete to crack along the height fully. Following this, the reinforcement starts to yield as the crack widens.

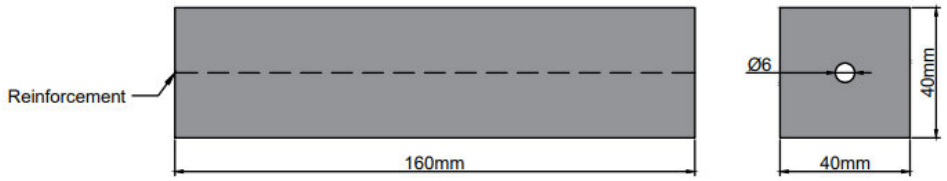

Figure 6.2: Dimensions of the concrete prism

6.1.2. Setup

The setup is prepared for a four-point bending test as shown in figure 6.3. Two types of sensors are used. LVDTs are used to validate the data from RFV-2. The LVDTs are glued on the front and back surface of the prism. The RFV-2 sensors are glued on the front surface along LVDT-1 (figure 6.4). A two-compound glue is used to obtain a strong bond. It is critical to ensure that the sensors do not rotate or detach due to the impact of the load.

As a consequence of the placement of LVDTs, the sensor strip and magnet are placed from 6cm to 10 cm depending on an ideal location such that the setup stays intact. Owing to this, the magnitude of the magnetic field is lowered for samples 3 and 4. No notch is required for the specimen.

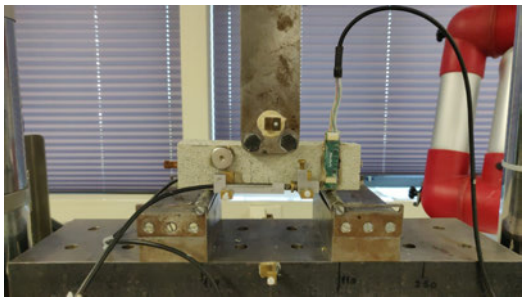

Figure 6.3: Experimental setup

6.1.3. Assumptions

1. Background field:
   The setup consists of using an INSTRON machine to apply load on the prisms. The equipment is made entirely of metal, contributing to a significant background field. Therefore, the background field is studied first to determine if the load cell eventually changes the magnetic field without the presence of a crack. It is found that lowering the load cell does not influence the readings. The background field is measured and subtracted from the total magnetic field to get the magnetic field from the magnet used. The explanation follows as given in section 5.2.
2. Crack width:
   Owing to the smaller size of the specimen, measurements from LVDTs show that the strain at crack initiation/failure is much smaller than the strain during crack propagation. The total displacement equals the sum of the crack width and the elastic deformation. When the elastic deformation is negligible, the total displacement found can be associated with the crack width.

$$\begin{aligned} \nabla_{total} &= \epsilon_e l + w \\ w &= \nabla_{total} - \epsilon_e l \end{aligned} \tag{6.1}$$

   Now,

$$\begin{aligned} \epsilon_e l &= 0.00966mm \approx 0 \\ \Rightarrow w &= \nabla_{total} \end{aligned} \tag{6.2}$$

3. Uniformity along thickness:
   For experiments which involve damage evolution, it is assumed that the crack propagation is uniform along the thickness. This is, however, not the case in a practical scenario. It is still assumed for simplification since the difference is not very high. For the zeroth experiment, the first and second LVDT measurement is shown in figure 6.5.

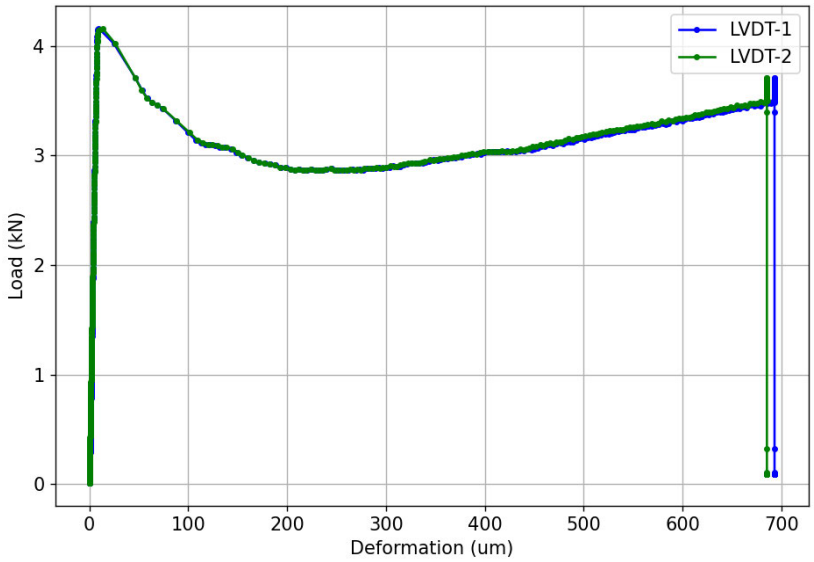

Figure 6.5: Measurements from LVDT-1 and LVDT-2

6.1.4. Background field

It is likely to assume that the experiment machine will cause the magnetic field to vary as explained in section 6.1.3. According to [48], the process of concrete cracking can influence the magnetic field intensity due to the piezoelectric effect and crack propagation effect. The study states that surface potential develops due to free charge in materials such as rocks, concrete and coal, which further induces a magnetic field. The study uses a fluxgate sensor which consists of a magnetic core, excitation coil, and induction coil. In this study, a permanent magnet and AMR sensor are used. Even so, checking if the concrete cracks contribute towards the magnetic field becomes essential. One sample is used to experiment in the absence of a magnet. The sensor is attached to measure the field. This field is referred to as the background field. Figure 6.6 shows the background field for the duration of the experiment. A non-linear plot is obtained due to the non-linearity error of AMR sensors and the dependency of the sensitivity of the sensors towards each component of the magnetic field [49]. It is found that the cracking process does not influence the magnetic field. If the factor for error is removed, a linear plot will be obtained, but this falls out of the scope of this study.

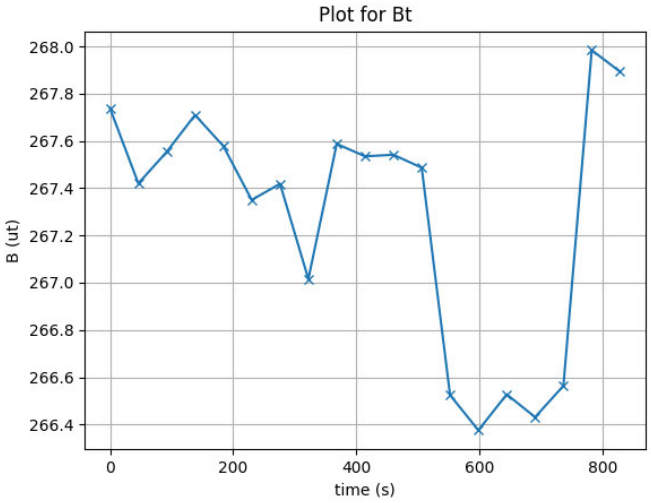

Figure 6.6: Background field

Time (s)	Total field (uT)
0	267.74
46	267.42
92	267.55
138	267.71
184	267.58
230	267.35
276	267.42
322	267.02
368	267.59
414	267.53
460	267.54
506	267.49
552	266.52
598	266.38
644	266.53
690	266.43
736	266.56
782	267.98
828	267.89

Table 6.1: Background field

6.1.5. Crack propagation

For this four-point bending test, a single crack will occur due to the bending of the prism. Up to 3 kN, the prism undergoes elastic deformation. A macro crack appears in the region between the loading points. A drop in the loading is realised at the crack initiation. The crack propagates over the height of the prism, and it

can be said that the concrete is cracked. However, the reinforcement now takes the load and steadily increases (Figure 6.7).

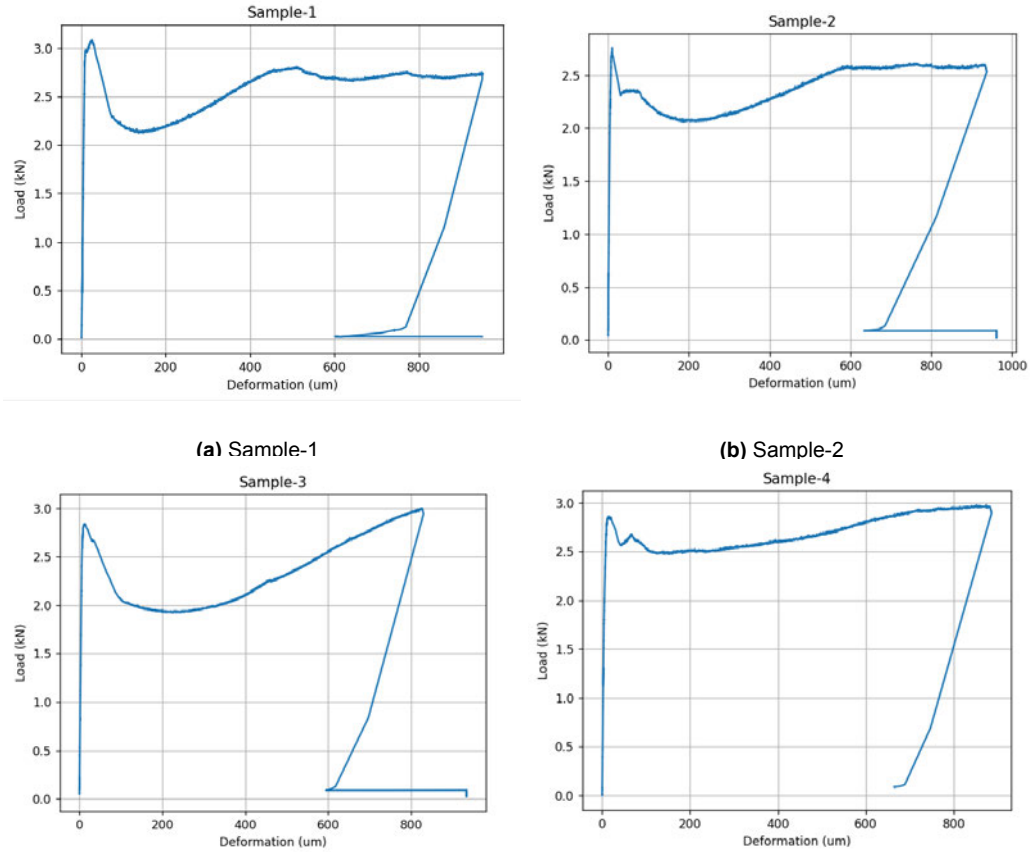

(a) Sample-1 **(b)** Sample-2

(c) Sample-3 **(d)** Sample-4

Figure 6.7: Load vs deformation curve

Experiment is stopped once the LVDTs display a deformation of 1000 μm. Therefore, the concrete cracks for all specimens, but the reinforcement is not fully yielding. The final drop in the graph is caused due to unloading of the specimen. In figure 6.7, the load vs displacement graphs for each sample from 1-4 is shown. A maximum load close to 3 kN is reached before failure. From figure 6.8, the deformation of the prism with time is illustrated.

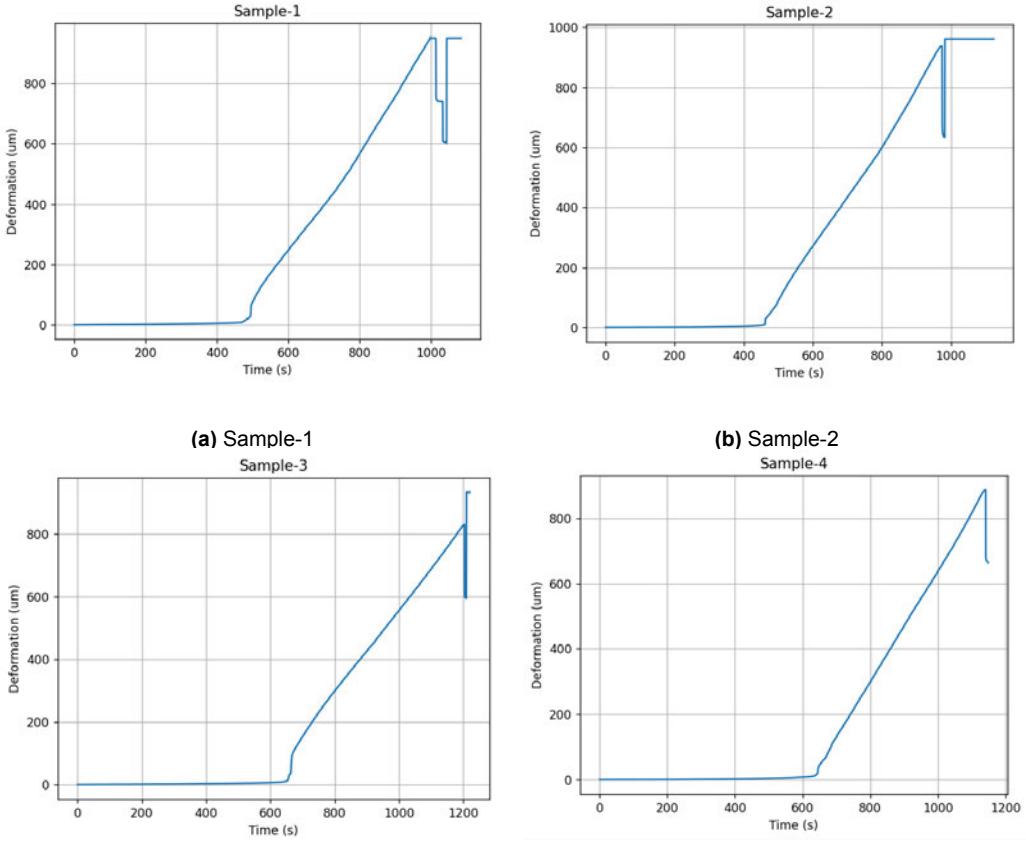

(a) Sample-1

(b) Sample-2

(c) Sample-3

(d) Sample-4

Figure 6.8: Deformation vs time curve

The deformation at peak load is approximately 9.66 μm. Further deformation occurs as the reinforcement starts to yield. The deformation will not exceed this value since the LVDTs can measure up to 1000 μm. The sampling rates of LVDTs and RVF-2 are different. Therefore, the LVDT readings are selected for the time when RFV-2 records reading to achieve qualitative analysis of the results. The sampling rate of RVF-2 is every 46 seconds. Whereas the sampling rate of LVDTs is every second. Since the time at which readings were taken is known for both, the LVDT readings are filtered accurately. Figure 6.9 plots the filtered readings from the LVDTs. From this, it becomes known at which time step the crack is initiated. The filtered readings are plotted against time in seconds.

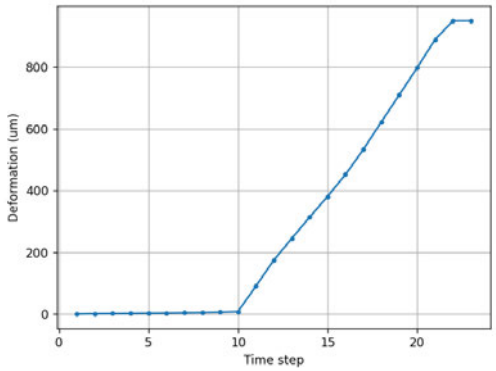

Figure 6.9: Filtered deformation

The magnetic field can be plotted against the deformation/crack-width as shown in figure 6.10a. During the elastic deformation stage, the deformation is in the order of $\leq 10\ \mu m$. The deformation before the onset of the crack is 8.08 μm. Due to the small magnitude, the magnetic field decreases without change in the deformation, making it difficult to visualise decreasing magnetic field during elastic deformation. Hence, the deformation is represented on a log scale as depicted in figure 6.10b. For discussion of results, two graphs are illustrated. One graph shows the magnetic field and deformation with time, and the second graph shows the correlation between the magnetic field and deformation.

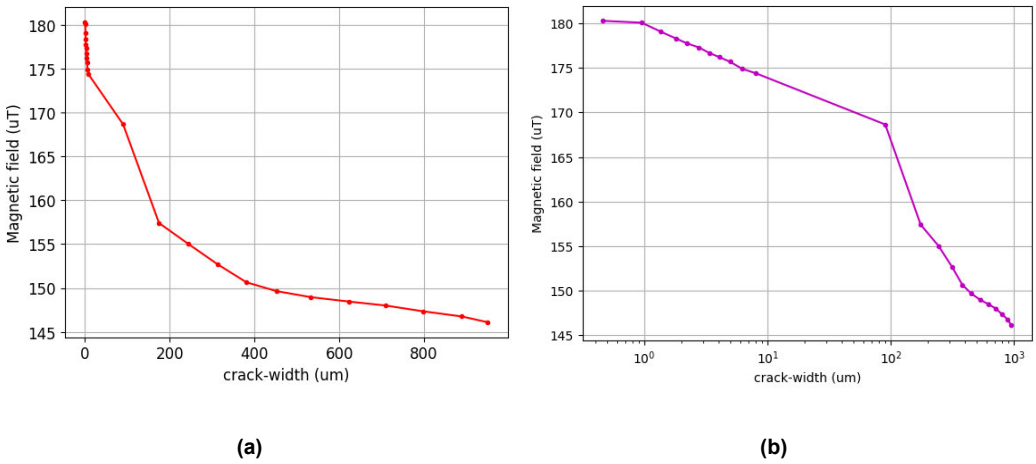

(a) **(b)**

Figure 6.10: Sample-1: (a) Magnetic field vs deformation (b) Magnetic field vs deformation on log scale

The correlation between the crack behaviour and magnetic field change is recorded in figures 6.12 to 6.15. When measuring the magnetic field, the field is observed to be decreasing as the deformation process begins. Small displacements due to elastic deformation affect the magnetic field. A larger jump in reading is observed at the time of crack initiation. This continues until the crack is developed across the height of the prism, i.e., propagation of the crack over the full height of the prism. After this, the crack has fully formed, and only the width increases as the reinforcement yields. The part where reinforcement starts yielding can be observed as the continuous uniform decrease at the end of the test. Therefore, from the experimental observations of the magnetic field behaviour, it can be concluded that using the RFV-2 sensors, different stages of the cracking process can be recognised. These are illustrated in figure 6.11.
Referring to figure 6.11, the elastic deformation is associated with the linearly decreasing magnetic field. A sudden reduction in magnetic field is observed on the onset of cracking. The region following the linear deformation is a representation of the crack formation. Once the crack has formed, it propagates towards the top of the prism. On the graph, it can be seen as another minor fluctuation followed by an almost linear trend. The concrete then fully cracks, and the curve moves towards steel yielding. Continuing the experiment until the reinforcement fails will give a plot of yielding. In this study, the system is developed as a monitoring system. However, in this experiment, crack detection was possible. The location of

the crack should be known to detect cracking which is not possible for practical application.

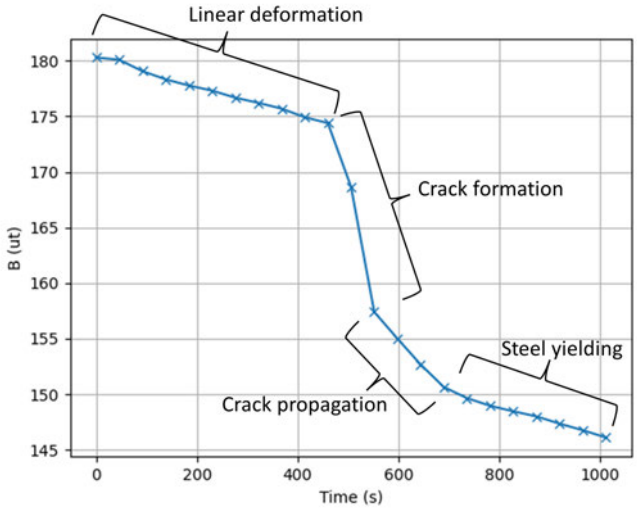

Figure 6.11: Phase division of crack process based on experimental analysis

The results obtained in sample-3 and 4 are lower in magnitude. The lower magnetic field is obtained due to the greater distance between the magnet and the sensor strip compared to samples 1 and 2. Another reason for a lower magnitude is the high background field. On reducing the background field, the remainder magnetic field was lower than 100 μT. Sample-3 resulted in an unprecedented observation. The jump, which indicated crack initiation, is observed, but other stages of continuous decrease in the magnetic field are not observed. Identifying the exact cause of this instance as the background field is completely removed from the test results proves challenging. One explanation that can be suggested for this behaviour is that the magnetic field is not constant throughout the experiment, and as a result, small reductions are expected. When the magnitude is in the order of hundreds (819µ being the upper limit for the sensors), these reductions are negligible. However, in the case of sample-3, the magnitude is lower, making it susceptible to being affected by these reductions. A similar observation is not recorded for sample-4, even though it falls under the same parameters. Therefore, the explanation cannot be confirmed. The sensor may have a region of sensitivity in which little changes in the magnetic field are easily recorded. Tests should be performed for different magnetic field ranges to determine the sensitivity region. This further study aims to identify the threshold above which the sensors will provide results consistent with samples 1, 2, and 4.

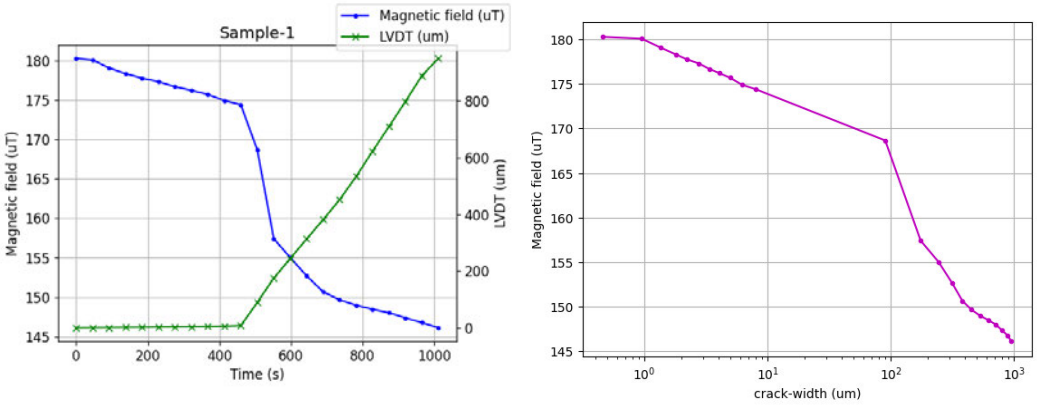

(a) (b)

Figure 6.12: Sample-1: (a) Changing magnetic field and displacement to time (b) Magnetic field vs displacement where the x-axis follows logarithmic scale

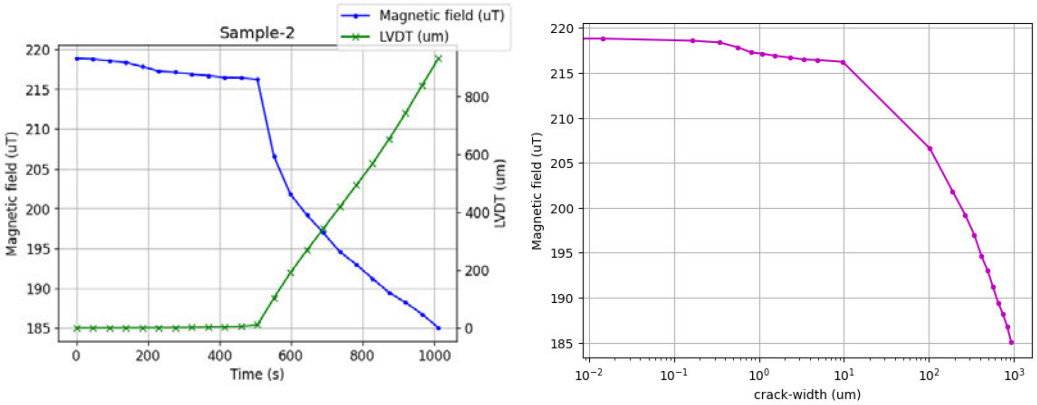

(a) (b)

Figure 6.13: Sample-2: (a) Changing magnetic field and displacement to time (b) Magnetic field vs displacement where the x-axis follows logarithmic scale

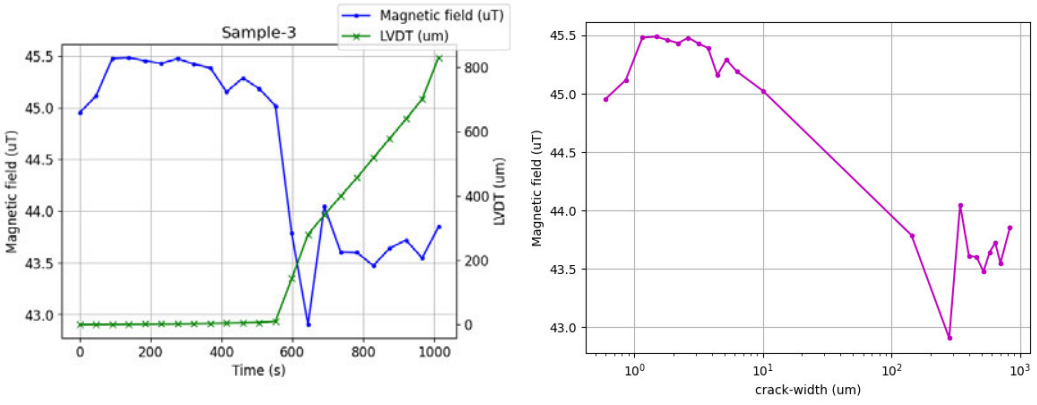

(a) (b)

Figure 6.14: Sample-3: (a) Changing magnetic field and displacement to time (b) Magnetic field vs displacement where the x-axis follows logarithmic scale

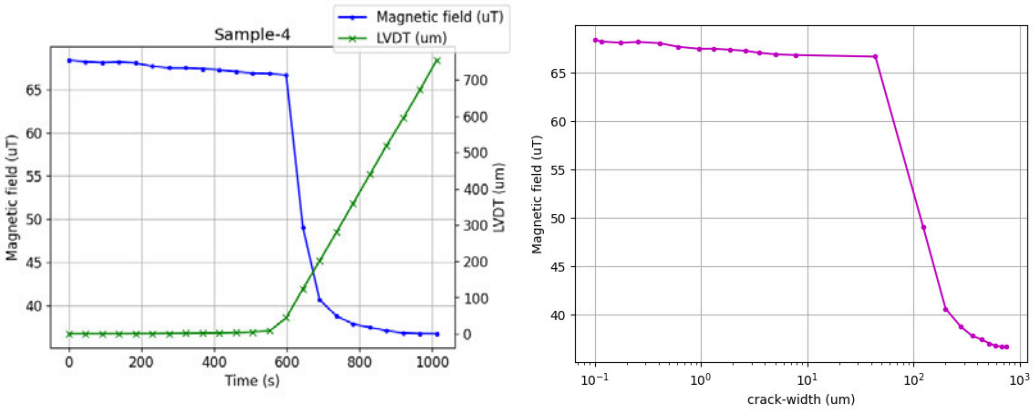

Figure 6.15: Sample-4: (a) Changing magnetic field and displacement to time (b) Magnetic field vs displacement where the x-axis follows logarithmic scale

7

Shear failure in a bridge girder

7.1. Flexure cracks in beams with shear reinforcement

In the previous section, the study of the qualitative correlation of magnetic field and crack width for a simple crack due to bending is performed. Variations like graphs are obtained when compared to the experiments using the moving table. Therefore, it becomes essential to study the nature of graphs for different crack types and varied boundary conditions. In this experiment, four-point bending is performed on a precast I-shaped girder. The plan of the experiment is shown in figure 7.2. The longer span of the beam is the region of interest for this experiment. Flexure cracking is expected initially, and the beam will undergo shear failure on other loading. The beam is part of the study ”Analytical and numerical models for the shear behaviour of precast concrete bridges at intermediate support” [50]. The beam discussed in this section has less than minimum shear reinforcement. Eurocode-2 provides the criteria for minimum shear reinforcement. The beam is subjected to loading with intermediate pauses.

The beam is set up with LVDTs, DIC and laser sensors to check the cracking. For RFV-2 sensors, DIC is used to validate the results. LVDTs are not used in this case as they will not result purely in the crack width. The load stages at which

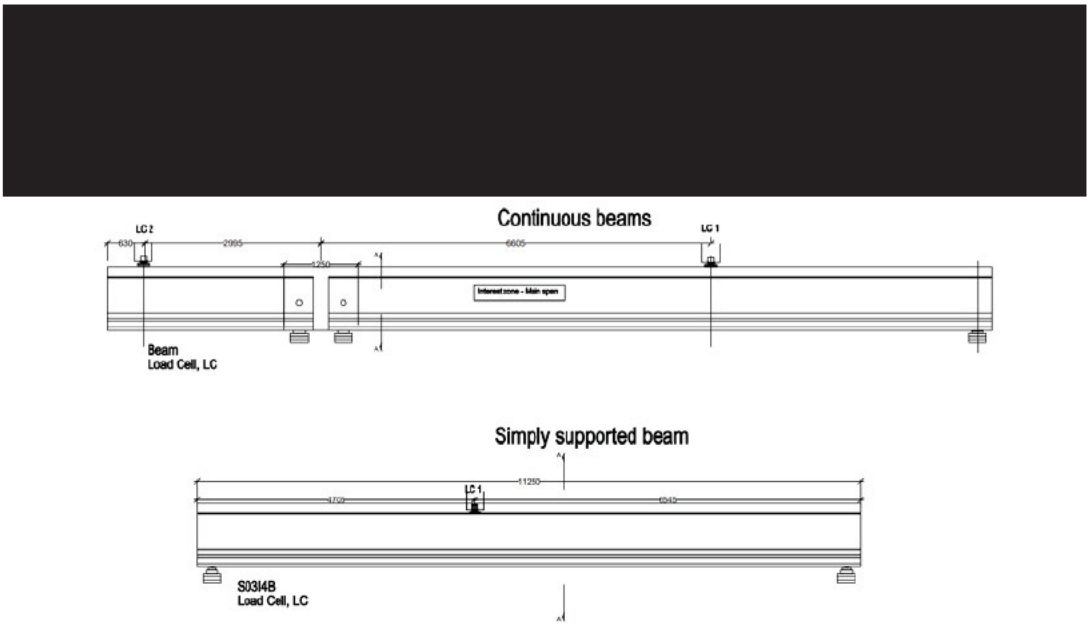

Figure 7.2: Loading plan of the beam

7.1.1. Setup

Flexure cracks are observed on the beam at a load value of 901.00 kN. The loading is paused at this point, and RFV-2 sensors are glued at the crack tip (Figure 7.1). Since it cannot be determined whether the crack will propagate further or not, 3 RFV-2 sensors are placed at three different crack tips. The crack tip along the 2nd RFV-2 sensor does not propagate further, whereas the third crack tip shows growth. Since the third crack and RFV-2 sensor were located in the flange, fewer data is available for processing the crack widths from Digital image correlation (DIC). For this section, results from 1st RFV-2 sensor are of primary focus.

7.1.2. Assumptions

1. The assumption of an average background field will also hold for this experiment. The sensor is placed at approximately $3cm$ from the magnet to receive a higher magnetic field. Doing so will eliminate the chances of external disturbances that will otherwise result in plot fluctuations. Due to the sufficient distance between the plate and the sensor, the effect on the magnetic field is negligible. However, as per the standard procedure for all experimental setups, the background field is removed from the measured magnetic field.
2. Another assumption is made for the cracking of the beam. From a practical point of view, it is possible to have nonuniform cracking along the thickness. However, assuming that the crack occurs uniformly across the thickness is standard practice. The sensors and DIC are positioned on opposite faces. The crack pattern from DIC is taken to be the same as what is obtained on the opposite face.

7.1.3. Crack propagation

The crack type expected in this experiment is flexure cracking leading to shear cracks, which will cause the failure of the beam. The test is representative of a bridge girder which can be a potential application of the RFV-2 sensors. In this case, the crack location cannot be determined before the experiment. The cracks are observed, and sensors are applied in those locations. In the case of a practical approach for bridge girders, multiple sensors can be applied in the region of expected failure. Out of these multiple sensors, some sensors can pick up the crack movement. It may also be possible to detect the cracks via the further research. figure 7.3 illustrates the crack propagation using strain in the beam based on images obtained from the DIC results.

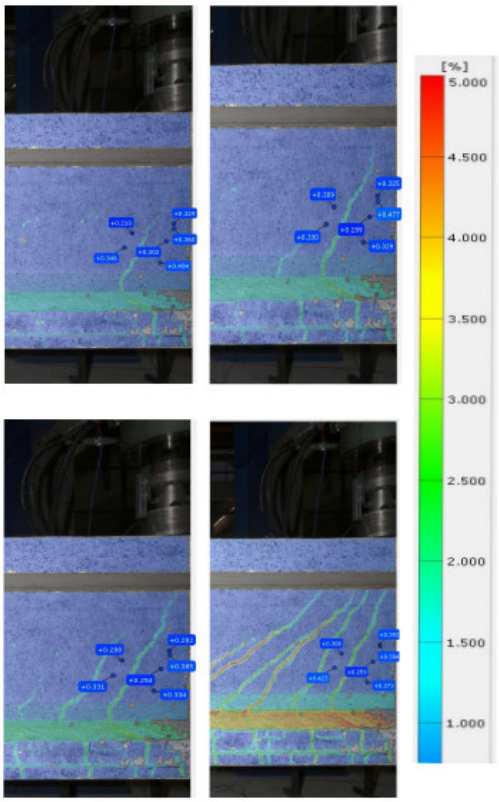

Figure 7.3: Strain evolution with increasing load as viewed using DIC

7.1.4. Results

figure 7.4 demonstrates the evolution of crack width with load and time. Furthermore, figure 7.4a illustrates how the crack progresses as the load increases. Since the sensor readings are time-dependent, the LVDT readings are plotted against time as shown in figure 7.4b. Figure 7.5a shows the variation in the magnetic field with respect to time for the entire experiment duration with the filtered values marked in yellow. The filtered values are shown in figure 7.5b. The filtered values occur at each load stage in the experiment. The magnetic field values must

be filtered for comparison since the DIC images are taken at each load stage.

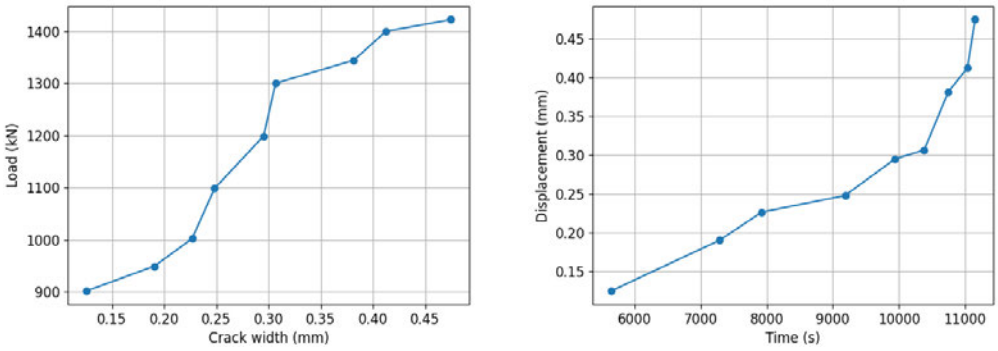

(a) Load vs crack-width **(b)** Crack-width vs time

Figure 7.4: Flexure cracking

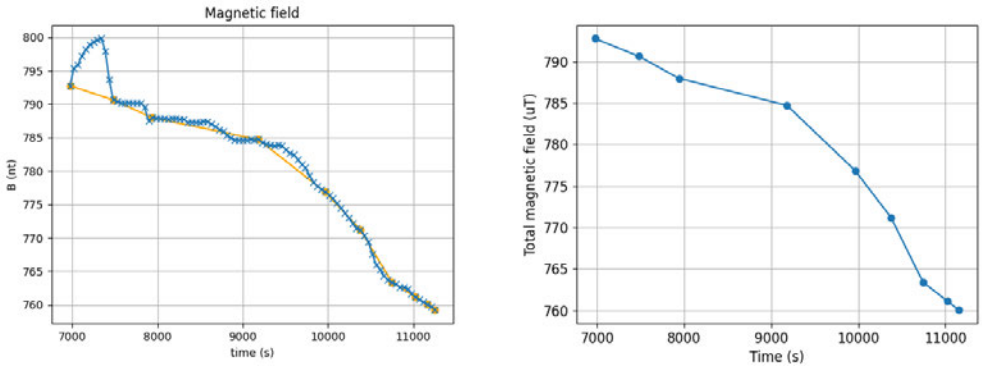

(a) Entire duration **(b)** Filtered time

Figure 7.5: magnetic field with time

When a crack is formed, it is possible that during a brief pause in loading, the crack undergoes closing and then opens again when loading is continued. This could explain the increase in magnetic field observed at the beginning of the experiment. Since the background field is subtracted from the magnetic field values, the plotted data purely reflects the results attributed to the presence of the magnet. The steady readings of the magnetic field at several intervals in the plot result from the loading discontinuity. In such cases, the crack does not undergo significant variation.

Figure 7.6 represents the correlation between the crack width and the magnetic field. To obtain the first dependence of the magnetic field with crack width, data from 7.4b is plotted against the filtered magnetic field 7.5. In Figure 6.12, a distinct jump in the measurement is observed at the initiation of the crack. Subsequently, a continuous drop in the magnetic field is observed. In this experiment, the sensor was applied after the formation of the crack, thereby excluding the jump in

value. The crack propagates for two load steps, after which it only grows in width until the total failure of the I-beam. It can be observed from the results that the magnetic field decreases as the crack widths increase.

8

Conclusions and Recommendations

This study highlights the significance of structural health monitoring of concrete structures, the limitations of the current techniques, and the requirement for a cost-effective and small-scale monitoring system. Traditional monitoring techniques, such as strain gauges, LVDTs and fibre optics, have drawbacks and necessitate the development of innovative approaches using various sensors. The proposed RFV-2 system delivers real-time data and enables the identification of cracks and the elastic behaviour observed from the experiments. It is an excellent long-term monitoring solution, and the wireless nature eliminates the need for physical inspection. The proposed monitoring system shows promise in addressing the challenges associated with crack monitoring in concrete structures. With further research and development, it might become a vital tool for SHM.
In this chapter, a comparison is drawn between the different analyses performed to develop the monitoring system, along with a detailed discussion of the obtained data using a critical approach. The chapter also deals with the limitations of the RFV-2 system at this introductory level. A conclusion is drawn for the main research question. Finally, recommendations and future work required are provided based on these limitations.

8.1. Comparative study

8.1.1. Numerical, analytical and experimental results

The study encompasses various analyses and experiments that collectively contribute to formulating the findings for the monitoring system RVF-2. The analytical and numerical approaches are conservative as they do not factor in external effects. Experimental data is considered the accurate result and should align with the theoretical-based FEM and equation-based calculation. Therefore, a comparison is made between the three different approaches. The final error percentage is calculated by accounting for average error at all data points.
The moving table experiment can be closely related to analytical and numerical analysis. Similarities arise because there is no background field in both the anal-

yses and the experiment, and the rate of distance change is constant in all three cases. Figure 8.1 depicts the magnetic field plotted for each case against the distance increased. An error of 4.45% is found. The FEM analysis and the analytical solution do not consider any external effects. They are solely dependent on the material's magnetic properties (in this case, permanent magnet).
For FE model,

$$B_r = \| B_r \| \frac{e}{\| e \|}$$
$$e = \begin{bmatrix} 0 \\ 0 \\ 1 \end{bmatrix} \tag{8.1}$$

From equation (4.6),

$$B_i = \frac{J}{\mu_0} \sum_{e=1}^{N} \sum_{i=0}^{1} \sum_{j=0}^{1} \sum_{k=0}^{1} (-1)^{i+j+k} f(i) \tag{8.2}$$
$$i = x, y, z$$

$f(i)$ = Function of distance in x,y,z

In equation (8.1), the remanent field and direction of magnetisation are known properties of the magnet. The FE analysis is based on these known parameters. From equation (8.2), it can be observed that the analytical solution is based on the parameter JA/m^2, which is the magnetisation of the permanent magnet. During the experiment, there is a background field due to the earth's magnetic field and the sensor itself. Even though the background field is removed from the data, some margin of error should be considered. In the case of engineering practices, it can be assumed that the sensors used are not perfect and may introduce errors

due to their inherent sensitivity. These factors combined will contribute to the total percentage of errors occurring.

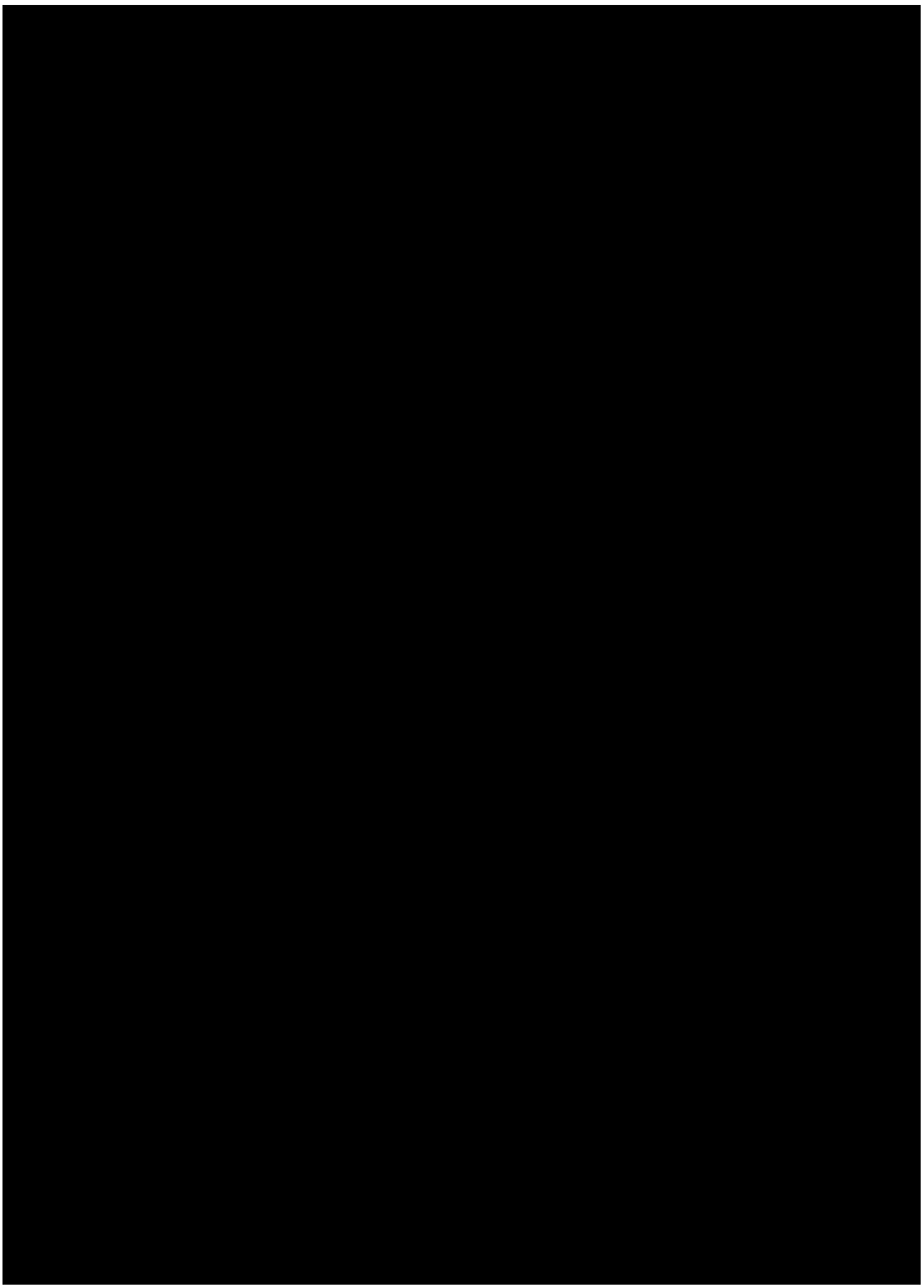

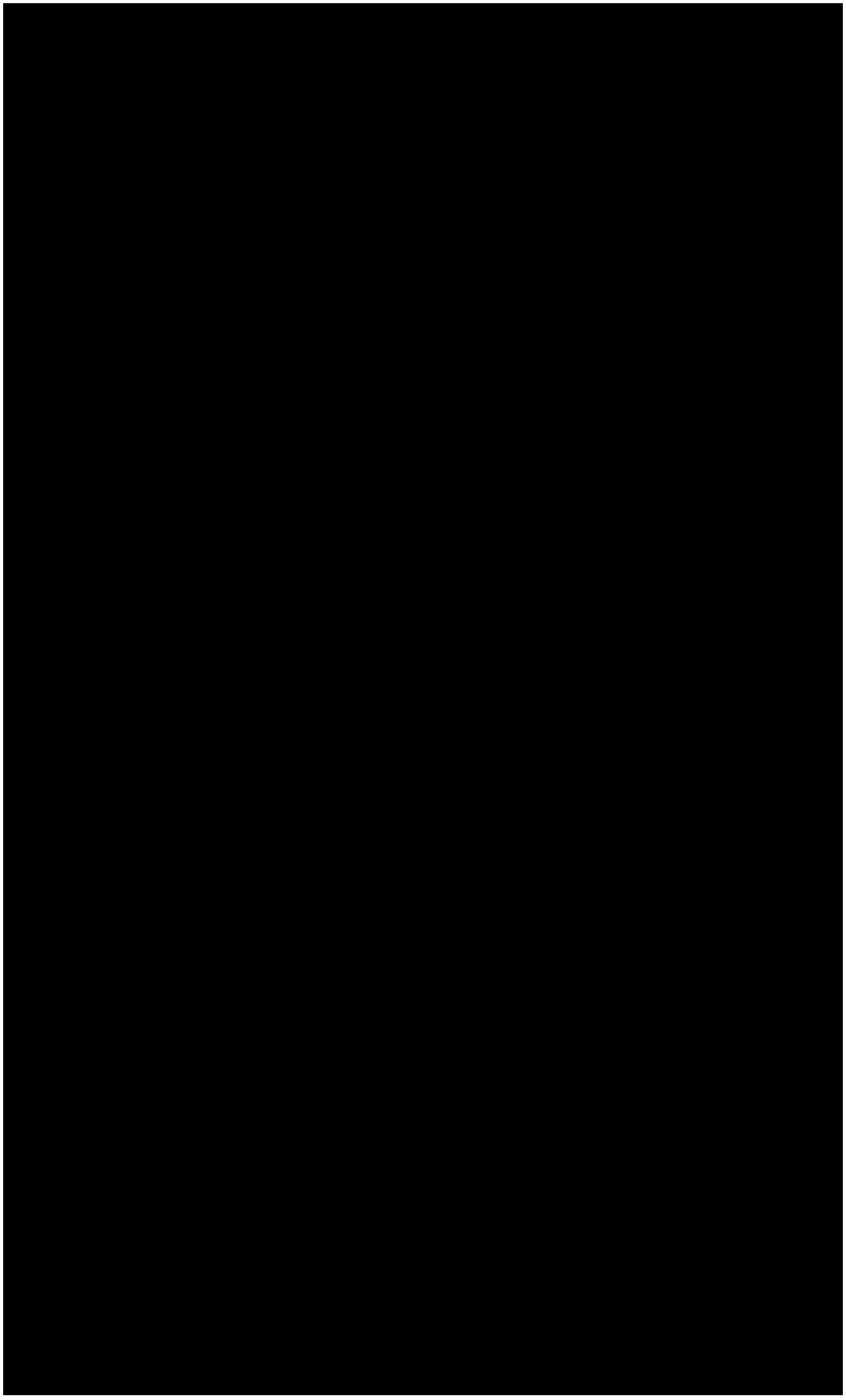

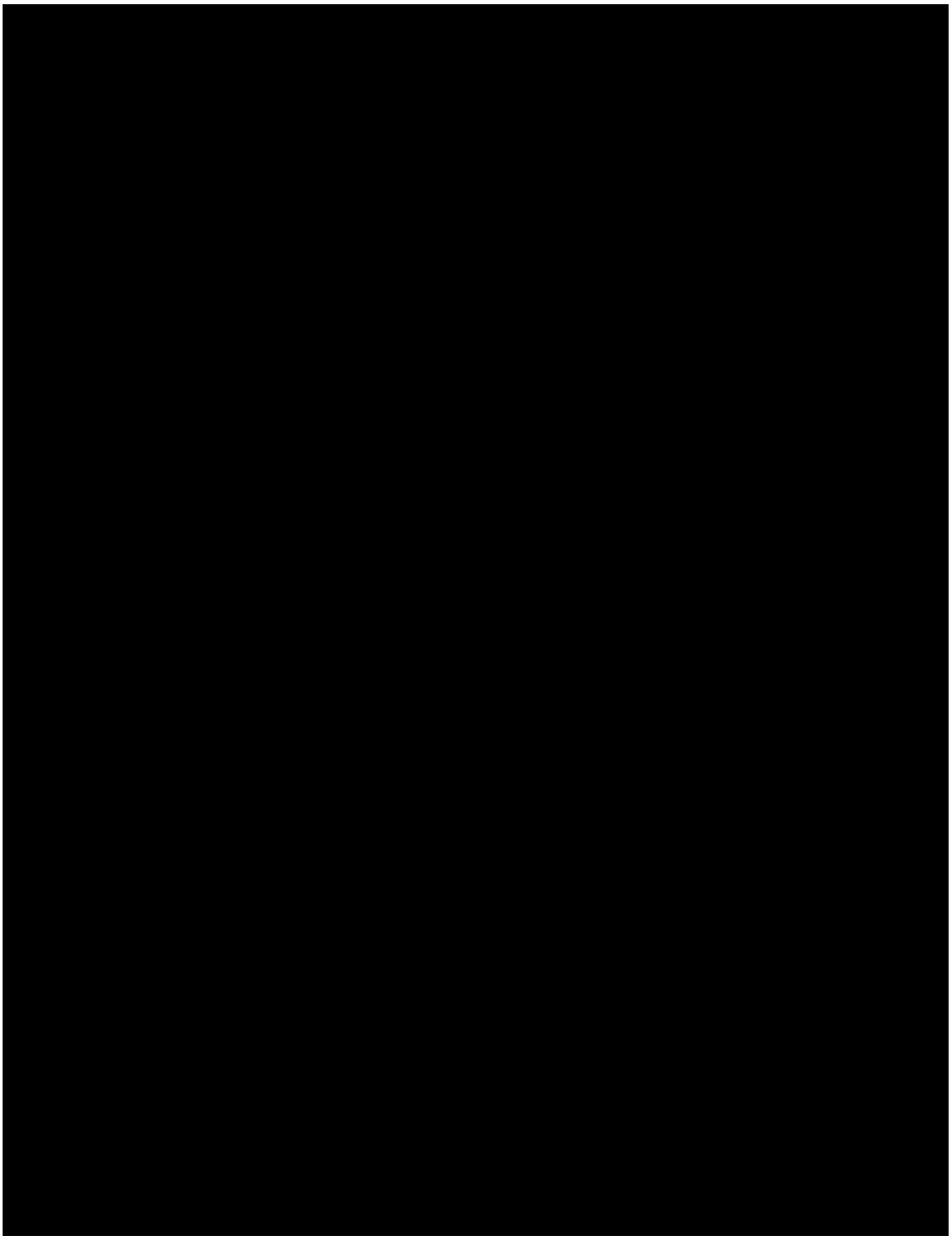

The first set of experiments, as explained in chapter 5, does not account for any material behaviour. These experiments are conducted solely in an air medium. However, there is speculation that the nature of the magnetic field will differ when the setup is placed on a concrete surface. Concrete exhibits initial elastic behaviour followed by plastic behaviour. As a result, the results differ from those obtained using the moving table experiments. An observation can be made by dividing the graph according to the different

phases of the cracking process. As mentioned in section 8.1.2, the initial decrease in the magnetic field is gradual, but subsequently, the difference in the magnetic field increases. Each segment of the graph can be described as nearly linear. Overall, the graph exhibits a pseudo-linear behaviour, similar to the pattern depicted in figure 8.4.

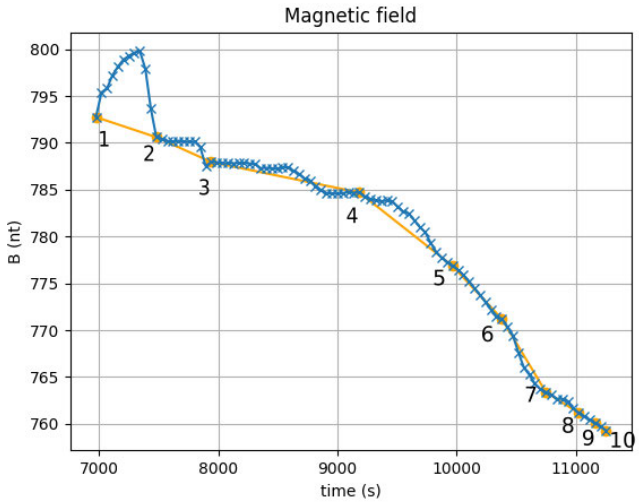

Figure 8.5: Load steps corresponding to the DIC readings taken for validation of sensors.

The third experiment, which focuses on the shear failure of a beam, yields even different results. The loading pattern should be understood first. The sensor readings are recorded after crack initiation, emphasising the increasing crack width. The test is designed in such a way that the loading is paused intermittently but not completely removed. As observed after the first load step, cracks may open and close in these cases, as depicted in figure 8.5. During load stage 3, the crack gradually widens, and after load step 5, the beam enters the failure zone, leading to larger crack widths.
To summarise, although the magnetic field follows inverse square law, the material behaviour of concrete plays an important role in the reduction of the magnetic field.

3. ***What is the level of precision of the sensor?***
The sensor operates from -819 µT to 819 µT. In Chapter 5, a repeatability experiment was conducted to measure the sensor's accuracy. The experiments resulted in a mean average error of 0.29%, implying that the sensors have high accuracy. Furthermore, a standard deviation of 0.79 was found. Herefore, the sensor readings deviate very slightly from the mean reading and with a low mean average error, implying that the accuracy of the monitoring system is acceptable.
For this study, a different accuracy level is established for the magnetic field in μT per unit distance. From the results in section 5.3, the magnetic field was decreasing at a rate of 87.56 $\mu T/mm$, and from section 5.4, it was found that the decrease in the magnetic field was 177.64 $\mu T/\mu m$. In the first case,

when the distance was measured in millimetres, the magnetic field reduction rate was higher compared to the second test, where the distance was measured in micrometres. These observations imply a correlation between the rate of change of distance and the rate of reduction of the magnetic field. Therefore, it is noteworthy to consider the scale of distance increment when studying the nature of the magnetic field.
Hence, the conclusion is in accordance with the inverse square law, which states that $B \propto \frac{1}{x^2}$, where B = Magnetic field and x = distance.

8.3. Limitations

During the experimental phase, several aspects of the sensors were tested. This led to the recognition of certain limitations affecting the current developmental stage of the monitoring system. The following limitations are formulated based on the observations:

1. **Dependency on visual inspection:** In the present prototype development stage, the monitoring system is limited to a single sensor and magnet. As a result, the ability to monitor cracks is contingent upon prior knowledge of their location. Visual inspection is required to identify the precise location of a crack before monitoring can be initiated. However, it should be noted that certain types of cracks, such as shear cracks, tend to occur abruptly, potentially rendering them difficult to monitor on time.
2. **Use of technique restricted to monitoring:** Building upon the previous point, the proposed technique within the system demonstrates its utility for crack monitoring. However, if the intention is to employ the technique for crack detection, an independent experimental analysis is required, employing multiple sensors. In the case of the four-point bending test case, successful crack detection was achievable due to the smaller specimen size and the prior knowledge that only a single crack would propagate. Therefore, it is essential to acknowledge that the current developmental stage of the technique limits its application primarily to monitoring rather than direct crack detection.
3. **Variation in monitoring system results:** The monitoring system yields varying results across different samples, making establishing a generalised relationship between the magnetic field and crack width challenging. Consequently, it becomes difficult to draw universal conclusions regarding this association.
4. **Calibration challenges:** The monitoring system will be susceptible to the influence of additional environmental factors, which might temporarily affect the measurements. These fluctuations pose a challenge for calibration purposes and require mitigation techniques. Robust calibration procedures can be implemented to minimise potential biases caused by external factors.

8.4. Recommendations and future work

The above conclusions and limitations suggest certain recommendations to refine the sensor results and fully utilise the monitoring system for practical applications.

1. **Expand the understanding of the nature of the magnetic field by performing more experiments.**
   In the study, three types of experiments are performed. Since it is established that the material behaviour affects the sensor readings, other material behaviour, such as softening and stiffening of reinforcement, crushing of concrete, and creep, should also be studied. By doing so, it becomes possible to assess the variation, like magnetic field reduction. Moreover, when utilising the monitoring system on-site, the type of crack can be determined.
2. **Design a layout with multiple sensors to locate and monitor cracks.**
   Currently, a single sensor was used to monitor a single crack. However, in practical scenarios, cracks can occur anywhere, and to effectively monitor such cracks, multiple sensors can be deployed over a region. A packet consists of a magnet, sensor, and magnet configuration. Another packet with a sensor, magnet, and sensor configuration can be made. When placed alongside each other, each sensor will be influenced by more than one magnet. This setup will ensure variation in measurement when a crack occurs. For example, multiple sensors can be placed in a grid formation in the monitoring region. The grid of sensors will provide data from various points, enabling the determination of the crack length and the prediction of its growth pattern. Further precision can be achieved by incorporating Bayesian analysis into the study.
3. **Improve the understanding of the accuracy of the sensor.**
   So far, there is a basic understanding of the sensor's accuracy. However, since the sensor readings differ for different samples, further studies can be conducted using multiple samples for all crack patterns. This will allow for the exploration of correlations within each crack pattern. Additionally, a study can be performed to determine the lowest value of the magnetic field at which the sensors become highly sensitive. This phenomenon was observed in sample-3, as discussed in section 6.1.5.

8.5. Scientific contributions

This study delivers a prototype for concrete structures' structural health monitoring system. The conclusions provided in the study demonstrate that the main objective of the study has been achieved. There is a gap in the literature regarding using an AMR sensor to monitor cracks in concrete. While several magnetic sensors are employed, they primarily rely on electromagnetic fields. Therefore, this study introduces a novel approach that addresses this gap and develops a new method for crack monitoring. Furthermore, the recommendations in this study can be implemented to transform it into a fully functional Structural Health Monitoring (SHM) system.

References

[1] A. Sofi et al. “Structural health monitoring using wireless smart sensor network – An overview”. In: *Mechanical Systems and Signal Processing* 163 (Jan. 2022), p. 108113. ISSN: 08883270. DOI: 10.1016/j.ymssp.2021.108113. URL: https://linkinghub.elsevier.com/retrieve/pii/S0888327021004957.

[2] Peter C. Chang, Alison Flatau, and S. C. Liu. “Review paper: Health monitoring of civil infrastructure”. In: *Structural Health Monitoring* 2.3 (2003), pp. 257–267. ISSN: 14759217. DOI: 10.1177/1475921703036169.

[3] Broek D. *The Practical Use of Fracture Mechanics*. URL: https://books.google.nl/books?hl=en&lr=&id=JFVtCQAAQBAJ&oi=fnd&pg=PR7&dq=broek+1988+fracture+mechanics&ots=zMp81mEHGs&sig=pm1Q8j1keG68LKTfoRdBRvIlowc&redir_esc=y#v=onepage&q=broek%201988%20fracture%20mechanics&f=false.

[4] Luigi Cedolin, Sandro Dei Poli, and Ivo Iori. “Experimental determination of the fracture process zone in concrete”. In: *Cement and Concrete Research* 13.4 (July 1983), pp. 557–567. ISSN: 0008-8846. DOI: 10.1016/0008-8846(83)90015-7.

[5] Petersson Erik. “Crack growth and development of fracture zones in plain concrete and similar materials”. In: ().

[6] Methi Wecharatana et al. “Predictions of nonlinear fracture process zone in concrete”. In: *Journal of Engineering Mechanics* 109.5 (1982), p. 109. ISSN: 1231-1246.

[7] CIE4160. *Textbook on Prestressed Concrete*. URL: https://brightspace.tudelft.nl/d2l/le/content/502155/viewContent/2775850/View.

[8] Annette Beedholm Rasmussen, Jakob Fisker, and Lars German Hagsten. “Cracking in flexural reinforced concrete members”. In: *Procedia Engineering* 172 (2017), pp. 922–929. DOI: 10.1016/j.proeng.2017.02.102. URL: www.sciencedirect.com.

[9] Shigenori Yuyama et al. “Quantitative analysis of fracture process in RC column foundation by moment tensor analysis of acoustic emission”. In: ().

[10] Z P Bazant and P A Pfeiffer. *Shear fracture tests of concrete*. Tech. rep.

[11] P S Chana. “Investigation of the mechanism of shear failure of reinforced concrete beams”. In: 39.141 (1987).

[12] “EN 1992-1-1: Eurocode 2: Design of concrete structures - Part 1-1: General rules and rules for buildings”. In: (2004).

[13] Kapilesh Bhargava et al. “Modeling of time to corrosion-induced cover cracking in reinforced concrete structures”. In: *Cement and Concrete Research* 35.11 (Nov. 2005), pp. 2203–2218. ISSN: 00088846. DOI: 10.1016/j.cemconres.2005.06.007. URL: https://linkinghub.elsevier.com/retrieve/pii/S0008884605001663.

[14] Dong Chen and Sankaran Mahadevan. “Chloride-induced reinforcement corrosion and concrete cracking simulation”. In: *Cement and Concrete Composites* 30.3 (Mar. 2008), pp. 227–238. ISSN: 0958-9465. DOI: 10.1016/J.CEMCONCOMP.2006.10.007.

[15] K Van Breugel. “Modelling in the service of sustainable construction”. In: 64.1 (2019).

[16] Aftab A. Mufti et al. “Civionics - A new paradigm in design, evaluation, and risk analysis of civil structures”. In: *Journal of Intelligent Material Systems and Structures* 18.8 (Aug. 2007), pp. 757–763. ISSN: 1045389X. DOI: 10.1177/1045389X06074572.

[17] Mayank Mishra, Paulo B. Lourenço, and G.V. Ramana. “Structural health monitoring of civil engineering structures by using the internet of things: A review”. In: *Journal of Building Engineering* 48 (May 2022), p. 103954. ISSN: 23527102. DOI: 10.1016/j.jobe.2021.103954. URL: https://linkinghub.elsevier.com/retrieve/pii/S235271022101812X.

[18] C. Sujatha. “Strain Gauge-Based Equipment”. In: *Vibration, Acoustics and Strain Measurement* (2023), pp. 305–349. DOI: 10.1007/978-3-031-03968-3{_}7. URL: https://link-springer-com.tudelft.idm.oclc.org/chapter/10.1007/978-3-031-03968-3_7.

[19] Yen-Chi Lu et al. “Metal strain gauges on membranes at large deflection J Li and W K Schomburg-New compliant strain gauges for self-sensing dynamic deformation of flapping wings on miniature air vehicles This content was downloaded from IP address 154 Recent advances in strain gauges”. In: 41 (1964).

[20] David S. Nyce. *Linear Position Sensors: Theory and Application*. URL: https://books.google.nl/books?hl=en&lr=&id=0SwbWS64c7UC&oi=fnd&pg=PR7&dq=related:4MxqG0R8RZ8J:scholar.google.com/&ots=Vorze47NEy&sig=ua_R0jDzeSlWxFmOu_AQIWPbL1c&redir_esc=y#v=onepage&q&f=false.

[21] Narendiran Anandan and Boby George. “Design and Development of a Planar Linear Variable Differential Transformer for Displacement Sensing”. In: *IEEE Sensors Journal* 17.16 (Aug. 2017), pp. 5298–5305. ISSN: 1530437X. DOI: 10.1109/JSEN.2017.2719101.

[22] Shang-Teh Wu, Szu-Chieh Mo, and Bo-Siou Wu. “An LVDT-based self-actuating displacement transducer”. In: *Sensors and Actuators A: Physical* 141.2 (Feb. 2008), pp. 558–564. ISSN: 09244247. DOI: 10.1016/j.sna.2007.10.027. URL: https://linkinghub.elsevier.com/retrieve/pii/S0924424707007376.

[23] C. I. Merzbacher, A. D. Kersey, and E. J. Friebele. “Fiber optic sensors in concrete structures: a review”. In: *Smart Materials and Structures* 5.2 (Apr. 1996), p. 196. ISSN: 0964-1726. DOI: 10.1088/0964-1726/5/2/008. URL: https://iopscience-iop-org.tudelft.idm.oclc.org/article/10.1088/0964-1726/5/2/008%20https://iopscience-iop-org.tudelft.idm.oclc.org/article/10.1088/0964-1726/5/2/008/meta.

[24] Liang Fan and Yi Bao. “Review of fiber optic sensors for corrosion monitoring in reinforced concrete”. In: *Cement and Concrete Composites* 120 (July 2021), p. 104029. ISSN: 0958-9465. DOI: 10.1016/J.CEMCONCOMP.2021.104029.

[25] Dimitrios G. Aggelis. “Classification of cracking mode in concrete by acoustic emission parameters”. In: *Mechanics Research Communications* 38.3 (Apr. 2011), pp. 153–157. ISSN: 0093-6413. DOI: 10.1016/J.MECHRESCOM.2011.03.007.

[26] Kentaro Ohno and Masayasu Ohtsu. “Crack classification in concrete based on acoustic emission”. In: *Construction and Building Materials* 24.12 (Dec. 2010), pp. 2339–2346. ISSN: 09500618. DOI: 10.1016/j.conbuildmat.2010.05.004. URL: https://linkinghub.elsevier.com/retrieve/pii/S0950061810002205.

[27] Fengqiao Zhang et al. “Developing a new acoustic emission source classification criterion for concrete structures based on signal parameters”. In: *Construction and Building Materials* 318 (Feb. 2022), p. 126163. ISSN: 0950-0618. DOI: 10.1016/J.CONBUILDMAT.2021.126163.

[28] Y. H. Huang et al. “Optical strain gauge vs. traditional strain gauges for concrete elasticity modulus determination”. In: *Optik* 121.18 (Oct. 2010), pp. 1635–1641. ISSN: 0030-4026. DOI: 10.1016/J.IJLEO.2009.03.002.

[29] Nick McCormick and Jerry Lord. “Digital Image Correlation”. In: *Materials Today* 13.12 (Dec. 2010), pp. 52–54. ISSN: 1369-7021. DOI: 10.1016/S1369-7021(10)70235-2.

[30] Christiane Maierhofer. “Nondestructive Evaluation of Concrete Infrastructure with Ground Penetrating Radar”. In: (). DOI: 10.1061/ASCE0899-1561200315:3287.

[31] Daniels David J. “Ground Penetrating Radar”. In: *IET radar, navigation and avionics series* (2007). URL: https://books.google.nl/books?hl=en&lr=&id=16PV-fhKasoC&oi=fnd&pg=PR15&dq=Daniels+D+(2004)+Ground+penetrating+radar,+2nd+edn.+The+Institution+of+Electrical+Engineers&ots=u-dCQlT9wc&sig=soiEDTYjxXofGfa_LRnZLBvRtUU&redir_esc=y#v=onepage&q&f=false.

[32] Kenneth R. Maser and W. M.Kim Roddis. “Principles of thermography and radar for bridge deck assessment”. In: *Journal of Transportation Engineering* 116.5 (1990), pp. 583–601. ISSN: 0733947X. DOI: 10.1061/(ASCE)0733-947X(1990)116:5(583).

[33] Ch Maierhofer et al. “Application of impulse-thermography for non-destructive assessment of concrete structures”. In: *Cement and Concrete Composites* 28.4 (Apr. 2006), pp. 393–401. ISSN: 0958-9465. DOI: 10.1016/J.CEMCONCOMP.2006.02.011.

[34] Muhammad Ali Salah et al. “Non-destructive assessment of concrete deterioration by ultrasonic pulse velocity: A review”. In: *IOP Conference Series: Earth and Environmental Science* 357.1 (Nov. 2019), p. 012015. ISSN: 1755-1315. DOI: 10.1088/1755-1315/357/1/012015. URL: https://iopscience-iop-org.tudelft.idm.oclc.org/article/10.1088/1755-1315/357/1/012015.

[35] Gábor Vértesy and Antal Gasparics. “Nondestructive Material Evaluation by Novel Electromagnetic Methods”. In: (2003). DOI: 10.4028/www.scientific.net/MSF.414-415.343. URL: www.scientific.net/MSF.414-415.343.

[36] Armin Dadras et al. *A Review on Non-Destructive Evaluation of Civil Structures Using Magnetic Sensors FONDECYT Initiation Project. Asphalt mixture with self-healing properties via microwave heating View project Designing Novel Meta-heuristics View project*. Tech. rep. URL: https://www.researchgate.net/publication/360318170.

[37] Gopel W., Hesse J., and Zemel J.N. *Sensors, a comprehensive survey*. URL: https://books.google.nl/books?hl=en&lr=&id=7I5FS4pJwekC&oi=fnd&pg=PP2&dq=magnetic+sensors+&ots=CB1LpiiGNX&sig=PX10km1bDLzc71L7ZJavRxYY-b8&redir_esc=y#v=onepage&q&f=false.

[38] Derk Jan Adelerhof and Wim Geven. “New position detectors based on AMR sensors”. In: *Sensors and Actuators A: Physical* 85.1-3 (Aug. 2000), pp. 48–53. ISSN: 09244247. DOI: 10.1016/S0924-4247(00)00341-1. URL: https://linkinghub.elsevier.com/retrieve/pii/S0924424700003411.

[39] Eric E. Fullerton and Jeff R. Childress. “Spintronics, Magnetoresistive Heads, and the Emergence of the Digital World”. In: *Proceedings of the IEEE* 104.10 (Oct. 2016), pp. 1787–1795. ISSN: 15582256. DOI: 10.1109/JPROC.2016.2567778.

[40] Igor Žutić, Jaroslav Fabian, and S. Das Sarma. “Spintronics: Fundamentals and applications”. In: *Reviews of Modern Physics* 76.2 (Apr. 2004), p. 323. ISSN: 00346861. DOI: 10.1103/RevModPhys.76.323. URL: https://journals-aps-org.tudelft.idm.oclc.org/rmp/abstract/10.1103/RevModPhys.76.323.

[41] Honeywell. *Magnetoresistive Sensors Application Note*. Tech. rep. 2003. URL: www.honeywell.com/sensing.

[42] Dongfeng He. “AMR Sensor and its Application on Nondestructive Evaluation”. In: *Magnetic Sensors - Development Trends and Applications* (Nov. 2017). DOI: 10.5772/INTECHOPEN.70334.

[43] Honeywell. *Application note handling sensor bridge offset*. Tech. rep. URL: www.magneticsensors.com.

[44] Pavel Ripka. “Magnetic sensors and magnetometers”. In: ().

[45] E P Furlani, S Reanik, and W Janson. “A Three-Dimensional Field Solution for Bipolar Cylinders”. In: *IEEE TRANSACTIONS ON MAGNETICS* 30.5 (1994). DOI: 10.1109/20.312547.

[46] Naamane Mohdeb, Hicham Allag, and Tarik Hacib. “A new approximation for calculating the attraction force in cylindrical permanent magnets arrays and cylindrical linear single-axis-actuator”. In: *Progress In Electromagnetics Research C* 91 (2019), pp. 213–225. ISSN: 19378718. DOI: 10.2528/PIERC19010804.

[47] *Magnetic field*. URL: https://www.magnetic-declination.com/Netherlands/Amsterdam/1856188.html.

[48] Shan Yin et al. “Experimental study on the change of magnetic field in the process of concrete failure under load”. In: *Structural Control and Health Monitoring* 28.10 (Oct. 2021). ISSN: 15452263. DOI: 10.1002/stc.2806.

[49] Pavel Ripka and Michal Janošek. “Advances in magnetic field sensors”. In: *IEEE Sensors Journal*. Vol. 10. 6. 2010, pp. 1108–1116. DOI: 10.1109/JSEN.2010.2043429.

[50] M S Ibrahim et al. “Challenges on the shear behavior of existing continuous precast girder bridges”. In: (2022), pp. 433–440. URL: https://www.openaccess.nl/en/you-share-we-take-care.